JGR Solid Earth

RESEARCH ARTICLE
10.1029/2020JB020999

The Lithospheric Architecture of Australia From Seismic Receiver Functions

Andrew Birkey[1], Heather A. Ford[1], Page Dabney[2], and Gillian Goldhagen[1]

[1]Department of Earth and Planetary Sciences, University of California – Riverside, Riverside, CA, USA, [2]Department of Geosciences, Princeton University, Princeton, NJ, USA

Key Points:

- Seismic discontinuities determined from Sp and Ps receiver function analysis
- Sp results agree with previous studies, but interpretations of negative phases in some places have changed
- Negative discontinuities seen from 50 to 150 km; lithosphere–asthenosphere boundary seen in younger regions, mid-lithospheric discontinuity in older (may be linked to ancient hydrous minerals)

Supporting Information:

Supporting Information may be found in the online version of this article.

Correspondence to:

A. Birkey,
abirk001@ucr.edu

Citation:

Birkey, A., Ford, H. A., Dabney, P., & Goldhagen, G. (2021). The lithospheric architecture of Australia from seismic receiver functions. *Journal of Geophysical Research: Solid Earth*, *126*, e2020JB020999. https://doi.org/10.1029/2020JB020999

Received 15 SEP 2020
Accepted 12 FEB 2021

Abstract In the past decade, mounting evidence has pointed to complex, layered structure within and at the base of the mantle lithosphere of tectonically quiescent continental interiors. Sometimes referred to as negative velocity gradients or midlithospheric discontinuities (MLDs), the origin of intralithospheric layering has prompted considerable discussion, particularly as to how they may result from continent formation and/or evolution. Previous Sp receiver function analysis in Australia (Ford et al., 2010, https://doi.org/10.1016/j.epsl.2010.10.007) found evidence for complex lithospheric layering beneath permanent stations located within the North, South, and West Australian Cratons and characterized these as MLDs. This study provides an update to the original study by Ford et al. (2010, https://doi.org/10.1016/j.epsl.2010.10.007). Sp receiver function results are presented for 34 permanent, broadband stations. We observe the lithosphere–asthenosphere boundary (LAB) on the eastern margin of the continent, at depths of 75–85 km. The cratonic core of Australia has discontinuities within the lithosphere, with no observable LAB. On the western margin of the continent, we observe several stations with an ambiguous phase that may correspond to an MLD or the LAB. We also observe multiple negative phases at most stations, suggesting a complex and heterogeneous lithosphere. Australian MLDs are likely linked to the presence of hydrous minerals in the midlithosphere and may result from ancient processes such as subduction, plume interaction, or melt infiltration from the paleo-LAB.

1. Introduction

1.1. Defining the Lithosphere–Asthenosphere Boundary and Midlithospheric Discontinuities

The lithosphere is the solid portion of the Earth that moves coherently over the convecting, plastic asthenosphere. Unlike the asthenosphere, the lithosphere is relatively rigid, due in large part to colder temperatures (Sleep, 2005), leading to faster seismic wave speeds. The transition from the lithosphere to the asthenosphere is referred to as the lithosphere–asthenosphere boundary (LAB), a region of the Earth's interior of particular interest because it is the most ubiquitous plate boundary and because the interaction between the lithosphere and asthenosphere has major implications for understanding plate tectonics and the dynamics of the mantle.

Different methods estimate somewhat different depths to this boundary due to differences in resolution and properties being observed. For example, in the Kaapvaal craton (an ancient, thick, stable continental core), xenoliths show the lithosphere to be 195–215 km thick (Eaton et al., 2009), while magnetotellurics suggests a thickness of ~230 km in the same region (Evans et al., 2011). In addition, there are differences in how the boundary is defined. Seismically, it is the velocity decrease from cold, fast lithosphere to warm, slow asthenosphere at 50 to >250 km (Fischer et al., 2010; Thybo, 2006). One common definition of the transition from lithosphere to asthenosphere is the point along a geotherm where temperature approaches the adiabatically determined mantle potential temperature (~0.9 T_M) and heat transfer changes from dominantly conduction in the lithosphere to convection in the asthenosphere (Sleep, 2005). In some regions, magnetotellurics can be used to determine the boundary between lithosphere and asthenosphere: very old lithosphere tends to be highly resistive due to depletion and dehydration during past melting events, while the asthenosphere below is generally more conductive (Baba et al., 2006; Eaton et al., 2009; Evans et al., 2005; Hirth et al., 2000). Dehydration and depletion couple with temperature to create a viscosity difference between layers: the cooler, dryer, more depleted lithosphere is more viscous than the hotter, wetter and more fertile asthenosphere (Hirth & Kohlstedt, 1996; Hirth et al., 2000; Karato & Jung, 1998; Lee, 2006; Lee et al., 2005; Sleep, 2005).

This viscosity difference may correspond to a change in strength as well, going from the mechanically stronger lithosphere to a weaker asthenosphere (Lee et al., 2005). Because the lithosphere is more viscous than the asthenosphere, strain will be localized at the base of the lithosphere. Thus, the LAB may also represent a change in anisotropy as plate motion aligns olivine at the base of the lithosphere (Gaherty et al., 1999; Levin & Park, 2000; Yuan & Romanowicz, 2010).

While the seismic LAB is a relatively sharp, discrete boundary in oceanic and Phanerozoic continental lithosphere, that is not the case in older lithosphere, where the LAB is frequently characterized as being transitional, extending over tens of kilometers (Abt et al., 2010; Fischer et al., 2010; Ford et al., 2010; Rychert et al., 2020). Thus, some authors instead refer to it as the lithosphere–asthenosphere transition (LAT; Mancinelli et al., 2017; Yoshizawa, 2014; Yoshizawa & Kennett, 2015). In cratonic regions where the lithosphere is thick, this transition occurs gradually over 60 km or more (Mancinelli et al., 2017). Both the depth of the LAB and how step-like the boundary appears to be are well correlated with tectonic age. Global tomography models show that regions of old continental crust (i.e., cratons) have fast seismic velocities to depths greater than 150 km, whereas younger, more tectonically active regions transition to slower seismic velocities at shallower depths (Auer et al., 2014; Nettles & Dziewoński, 2008; Ritsema et al., 2011; Schaeffer & Lebedev, 2013). One promising avenue of investigation has been the use of Sp and Ps receiver functions (RFs) to image the interface between lithosphere and asthenosphere. RFs rely on conversions between *P* and *S* waves at sharp seismic boundaries; a velocity decrease with depth can be observed as a positive pulse, while a velocity decrease with depth can be observed as a negative pulse (see Figure 3). This method has allowed for the high-resolution imaging of seismic discontinuities in the lithosphere including the Moho and the LAB. Rychert and Shearer (2009) used this technique to globally image the LAB, observing a negative boundary between 70 and 100 km. Other RF studies have observed the LAB in cratonic regions at depths of up to 250 km, and oftentimes no LAB is observed (Abt et al., 2010; Ford et al., 2010; Hopper & Fischer, 2015; B. L. N. Kennett et al., 2017; Shen et al., 2019; Sodoudi et al., 2013).

Regions of particularly thick lithosphere have been shown to possess velocity decreases of 5%–7% at depths between 80 and 150 km, above the seismically estimated LAB in such regions (Carlson et al., 2005; Griffin et al., 2009; Schaeffer & Lebedev, 2013). These discontinuities are usually termed midlithospheric discontinuities (MLDs). Abt et al. (2010), Fischer et al. (2010), and Ford et al. (2010) first termed these discontinuities as MLDs, but they had been observed previously (Chen, 2009; Dueker et al., 2001; Hales, 1969; Rychert & Shearer, 2009; Thybo, 2006; Wittlinger & Farra, 2007) and have since been observed in numerous cratons (Bodin et al., 2014; Ford et al., 2016; Foster et al., 2014; Hansen et al., 2013; Hopper & Fischer, 2015; Hopper et al., 2014; B. L. N. Kennett et al., 2017; Kind et al., 2012; Kumar et al., 2012; Lekić & Fischer, 2014; Porritt et al., 2015; Selway et al., 2015; Shen et al., 2019; Sodoudi et al., 2013; Sun et al., 2018; Wölbern et al., 2012) and even in some regions of anomalously thick oceanic lithosphere (Tharimena et al., 2016). In some cases, these discontinuities are continuous across Precambrian terrane boundaries, but in others they vary within terranes and across boundaries. Some hypothesize that MLDs may have formed as a result of cratonic thickening during the closure of ocean basins in the Precambrian, representing the scars of ancient and prolonged deformation within and at the base of the lithosphere (Cooper & Miller, 2014).

Despite MLDs being nearly ubiquitous in cratons, there is much debate as to their origin. It is clear that they are not the result of any obvious phase transitions (Carlson et al., 2005; Griffin et al., 2009). Mechanisms that have been invoked to explain them include partial melt (Kumar et al., 2012; Thybo, 2006), ancient solidified magma (Rader et al., 2015), partial melt in thermally perturbed cratons (Aulbach, Massuyeau, & Gaillard, 2017), elastically accommodated grain-boundary sliding (Karato, 2012), changes in Mg# (Yuan & Romanowicz, 2010), hydrous minerals (Hopper & Fischer, 2015; Selway et al., 2015), or anisotropy (Rychert & Shearer, 2009; Wirth & Long, 2014). In Section 4.3, we explore the potential mechanisms responsible for MLDs in craton Australia.

1.2. Continental Tectonics and Observed Seismic Structure

Australian lithosphere preserves a long and complex tectonic history. The western two thirds of the continent consists of Archean and Proterozoic cratons, while the eastern third is dominantly Phanerozoic-aged orogens (Figure 1). Precambrian Australia is generally divided into the West Australian Craton (WAC), the North Australian Craton (NAC), and the South Australian Craton (SAC). Most components of these cratons

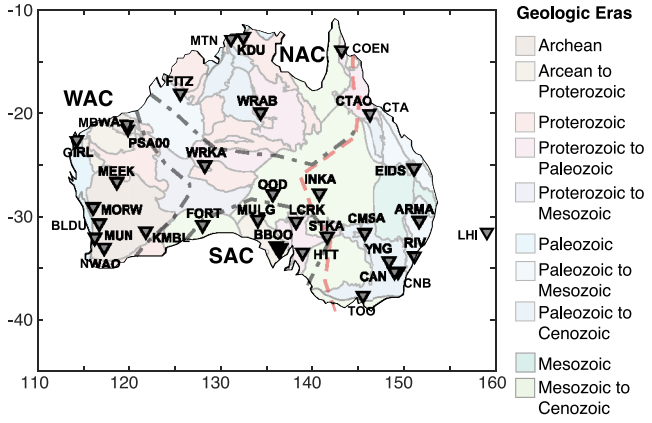

Figure 1. Map of significant geologic divisions of Australia, simplified from Fraser et al. (2007). Labeled are the West Australian Craton (WAC), the North Australian Craton (NAC), and the South Australian Craton (SAC). Inverted triangles are stations used in this study. Station names are shown in Figure 3. The red dashed line represents the Tasman Line, based on Direen and Crawford (2003).

were formed by roughly 1.8 Ga and were sutured together by the Neoproterozoic as part of the supercontinent Rodinia (Betts et al., 2002; Cawood & Korsch, 2008). The amalgamation of these cratons can be observed seismically throughout central Australia as lower wave speeds above 80 km, and anomalously strong radial anisotropy (Sun & Kennett, 2016; Wei et al., 2018; Yoshizawa, 2014; Yoshizawa & Kennett, 2015). In general, these cratons are thicker, colder, denser, and more depleted than the Phanerozoic east, with a gradational seismic LAB and MLDs at depths between 70 and 90 km (Debayle & Kennett, 2000; Fichtner et al., 2010; Fishwick & Rawlinson, 2012; Fishwick & Reading, 2008; Fishwick et al., 2005; Ford et al., 2010; Tesauro et al., 2020; Yoshizawa, 2014; Yoshizawa & Kennett, 2015).

1.2.1. West Australian Craton

The WAC is composed of the Yilgarn and Pilbara Cratons, which both locally preserve Archean crust in granite-greenstone belts (Barley et al., 1998; Betts et al., 2002; Myers, 1993). These cratons are due not exceed ~800°C down to 200 km and are highly depleted (Mg# > 90.5) with a strongly resistive cratonic root (Sun et al., 2018; Tesauro et al., 2020; L. Wang et al., 2014). Proterozoic orogens between the two cratons display a deepened, gradational Moho and complex upper crust; the cratons have a shallower, sharper Moho and simple crustal structure, with a thickened Moho (~40 km) in the Northern Yilgarn (Reading & Kennett, 2003; Reading et al., 2007, 2012). Additionally, the terranes of the WAC appear to have distinct crustal wave speeds, implying that these were set properties before amalgamation (Reading et al., 2007). The seismic LAB in the WAC is likely very deep, with tomography estimating a potential depth of 100 to >250 km (Yoshizawa & Kennett, 2015). Previous RF studies have observed MLDS at KMBL, MBWA, and NWAO between 70 and 85 km, with a potential LAB at NWAO at 164 km (Ford et al., 2010; Kumar et al., 2007).

1.2.2. North Australian Craton

The NAC is composed predominantly of Proterozoic basins rimmed by orogens (Betts et al., 2002; Cawood & Korsch, 2008; Myers et al., 1996). This region is typified by thick, depleted lithosphere (~200 km and Mg# 90.5), with complex midlithospheric structure, and low attenuation (B. L. N. Kennett & Abdullah, 2011; B. L. N. Kennett et al., 2017; Tesauro et al., 2020). There is a marked contrast between the eastern edge of the NAC and the Phanerozoic Thomson Orogen, with the former having thicker crust (B. L. N. Kennett & Liang, 2020). Earlier RF studies observed MLDs at FITZ and WRAB at 81 km and the LAB at 180 km (Ford et al., 2010; Kumar et al., 2007).

1.2.3. South Australian Craton

The SAC has some Archean gneissic terranes in the Gawler Craton, rimmed by Proterozoic orogens and basins (Cawood & Korsch, 2008; Conor & Preiss, 2008; Daly, 1998). Unlike the other Australian cratons, the SAC has a higher temperature, thinner lithosphere with slower wave speeds, and a more enriched mantle (Mg# ~89.5); enrichment has been interpreted as due to the possible refertilization of the mantle during the Proterozoic, while the thinned lithosphere is more likely due to the detachment of the SAC from Antarctica (Rawlinson et al., 2016; Tesauro et al., 2020; Yoshizawa & Kennett, 2015). Despite these differences, there is still a marked change between the SAC and Phanerozoic lithosphere to its east, with a thickening of the Moho and seismic lithosphere to the west accompanied by changes in reflectivity (Liang & Kennett, 2020). Ford et al. (2010) observed an MLD at FORT at 79 km, while BBOO and STKA both had a visible LAB at 131 and 104 km, respectively.

1.2.4. Phanerozoic Australia

Separating the Precambrian west and the Phanerozoic east is the Tasman Line: predominantly defined by surface geology, this line may be linked to the breakup of Rodinia (Direen & Crawford, 2003). There is a sharp transition in wave speeds at depth between the east and west, but it is further to the east than most

proposed models of the Tasman Line, suggesting a complex transition at depth between terranes of varying age (B. L. Kennett et al., 2004). Following the breakup of Rodinia, successive orogenic events accreted new lithosphere onto the cratonic core over a roughly 500 million-year time span (Betts et al., 2002). During the Cenozoic, Australia drifted north-northeast over a potential mantle plume, resulting in volcanic chains along the eastern margin that can be observed as lower seismic velocities and a shallower seismic LAB (Davies et al., 2015; Ford et al., 2010; Rawlinson et al., 2016; Wei et al., 2018). In contrast to most of the Precambrian west, eastern Australia has thinner, warmer lithosphere increasing stepwise to the west with a well-defined LAB between 70 and 100 km (Demidjuk et al., 2007; Fishwick & Reading, 2008; Ford et al., 2010).

2. Data and Methods

2.1. Data and Data Preprocessing

To begin the updated analysis of lithospheric structure of Australia, data were requested for 88 stations from five networks (AU, G, IU, II, and S1). Data requests were limited to data archived at the Incorporated Research Institutions for Seismology (IRIS) Data Management Center. Data were also requested from network S1 (Seismometers in Schools): ultimately none of these stations produced Sp receiver functions of sufficient quality to be included in the results section. Our final selection of 35 stations is an increase of 17 from Ford et al. (2010), with 10 years of additional data. On average, our Ps receiver functions had 950 events, while Sp receiver functions had 245 stations per event. There was an average increase of 238 events per station for Sp results, and a 1,040 event increase for Ps results. To prepare the data for later analysis, seismograms were quality controlled to ensure continuity with no gaps or spikes, initially filtered from 0.01 to 9.9 Hz and rotated from north and east into radial and transverse components. Once completed, direct P and S phases were selected by automated algorithm, a procedure originally described in Abt et al. (2010). From there, the data were rotated again into the P-SV-SH coordinate system. This rotation minimizes the amount of parent phase energy on the daughter component. The method used in this study follows from Abt et al. (2010) with minor variations to account for multiple stations in proximity using an array-based procedure as described in Lekić and Fischer (2014).

2.2. The Calculation of Ps and Sp Receiver Functions

Sp receiver functions were band-pass-filtered to 0.03–0.5 Hz and limited to events occurring within an epicentral distance window of 55°–75° and depths of less than 300 km since the direct S phase often arrives very close in time to other phases, and these constraints allow for the highest likelihood of isolating converted phases (Wilson et al., 2006). The deconvolution to generate the Sp receiver functions was performed using an extended-time multitaper (ETMT) cross-correlation method (Helffrich, 2006), which builds upon the multitaper method of Park and Levin (2000), with the added benefit of preserving the amplitude of phases at all depths within our study.

RFs were stacked by station to enhance the signal-to-noise ratio of discontinuity phases. When binning per station, individual RFs are normalized relative to the amplitude of the parent phase: this allows us to more directly compare amplitudes from different stations. An important substep of this process is to determine the statistical robustness of the resulting RF. To achieve this, a bootstrapping analysis is performed on the data. The published results are the mean of the RFs generated through the bootstrap analysis. The data set is also used to calculate two sigma uncertainties at each depth, allowing us to determine the uncertainties in RF phase depth and amplitude. In order to correct for variations in arrival time as a function of distance and to migrate the RFs to depth, the Australian Seismological Reference Model (AuSREM) was used (Kennett & Salmon, 2013). AuSREM has a crustal component (Salmon et al., 2013) which includes Vp and Vs and was determined from earlier RF studies, seismic refraction, reflection and tomography. A complete list of the references used to generate the crustal component of AuSREM can be found in Table 2 of Salmon et al. (2013). The mantle component of AuSREM (Kennett et al., 2012) provides values of Vp and Vs, gridded in 0.5° increments in latitude and longitude, and 25 km increments in depth from 75 to 300 km. The model itself was generated using data from a variety of surface wave, body wave, and regional tomography models from the region.

Before moving on it should be noted that a common concern of Sp receiver function analysis in the application of imaging mantle structure is the potential that the negative phase observed immediately beneath the Moho phase is a sidelobe of that positive phase. In Lekić and Fischer (2017), it was demonstrated that sidelobes can become an issue in instances where Sp receiver functions are calculated using frequency domain methods such as ETMT, which we use in this study. However, when the results are not bandwidth limited (e.g., the upper corner frequency limit extends beyond 0.125 Hz) and post-S arrivals are excluded (as we do here), this should not be an issue. More qualitatively, we observe no correlation between the depths of the Moho and negative phases (Figure 6), as might be expected if the negative phase were a sidelobe of the Moho phase (i.e., deeper Moho phase produces a sidelobe with a deeper negative phase).

Ps receiver function results were also calculated in this study. The Ps receiver functions were calculated in a method similar to that described above for Sp receiver functions. Exceptions to this are that the Ps receiver functions were filtered to 0.02–2 Hz and limited to epicentral distances of 35°–80° with no hypocenter depth cutoff. Additionally, while the Sp receiver functions published in this study are flipped in time and polarity reversed, no such corrections are needed for Ps receiver functions. Due to potential interference from crustal reverberations, the Ps receiver functions are not used to constrain potential mantle interfaces, which is the focus of our study. However, we do include them in our results in order to demonstrate the robustness of inferred Moho depths from AuSREM (Section 3.1).

This study presents an updated catalog of Sp receiver function results from the earlier study by Ford et al. (2010). The methodology here is similar with minor variations. Both studies utilize the same data preparation, coordinate system (P-SVSH) rotation, and waveform windowing described in Abt et al. (2010). Both also employ the same epicentral distance and depth cutoffs. The biggest methodological differences are in the deconvolution methods and in the migration models used. In Ford et al. (2010), all waveforms were simultaneously deconvolved and migrated using a frequency domain, water-level stabilized deconvolution (Bostock, 1998). The migration model varied from station to station, using H-k stacking (Zhu & Kanamori, 2000) to determine the crustal velocities and applying a uniform mantle model of AK135 (Kennett, 1995) at all stations. In our updated study, we individually deconvolve each waveform using an ETMT cross-correlation method (Helffrich, 2006) and later stack and migrate the receiver functions using the AuSREM velocity model. Because AuSREM is a local model, it provides us with better constraints for the Australian continent than utilizing H-k stacking for the crust and a global mantle model such as AK135. A final important distinction is that our study has more data, providing an extra decade of data compared to Ford et al. (2010), and allowed for the use of stations which previously only had a few years of data, increasing the number of stations analyzed for mantle structure from 14 to 34.

3. Results

3.1. Ps Receiver Function Results

As mentioned above, Ps receiver functions are not commonly used to image upper mantle discontinuities because of contamination from crustal reverberations. However, they are particularly sensitive to the Moho discontinuity and thus they are a useful independent constraint on Moho depths estimated from other methods, including Sp receiver functions. Throughout most of Australia, the Moho as estimated by Ps receiver functions falls between 35 and 45 km, with seven stations having a deeper Moho (Figure 2). In addition, the thickness of the crust seems to be in rough agreement with the age and local geology (i.e., particularly thick crust is seen in the cratons and Proterozoic orogens, with much thinner crust in the Phanerozoic east).

Figure 2 shows both the misfit between the depth to Moho as predicted by AusMoho (B. L. Kennett et al., 2013; Salmon et al., 2013) and the depth to Moho as determined from our Ps RFs. AusMoho is a compilation of data from multiple seismic methods (i.e., refraction and reflection studies, RFs, and tomography). The Moho was defined as the point below which compressional velocities are greater than 7.8 km/s and shear velocities are greater than 4.4 km/s; a grid was constructed for the continent using the weighted interpolation of data from different sources depending on the quality of the individual method (B. L. Kennett et al., 2013; Salmon et al., 2013). Most stations have a misfit of 4 km or less. Additionally, it is worth noting that at most stations there was a negative misfit, meaning that AusMoho overestimated the depth to

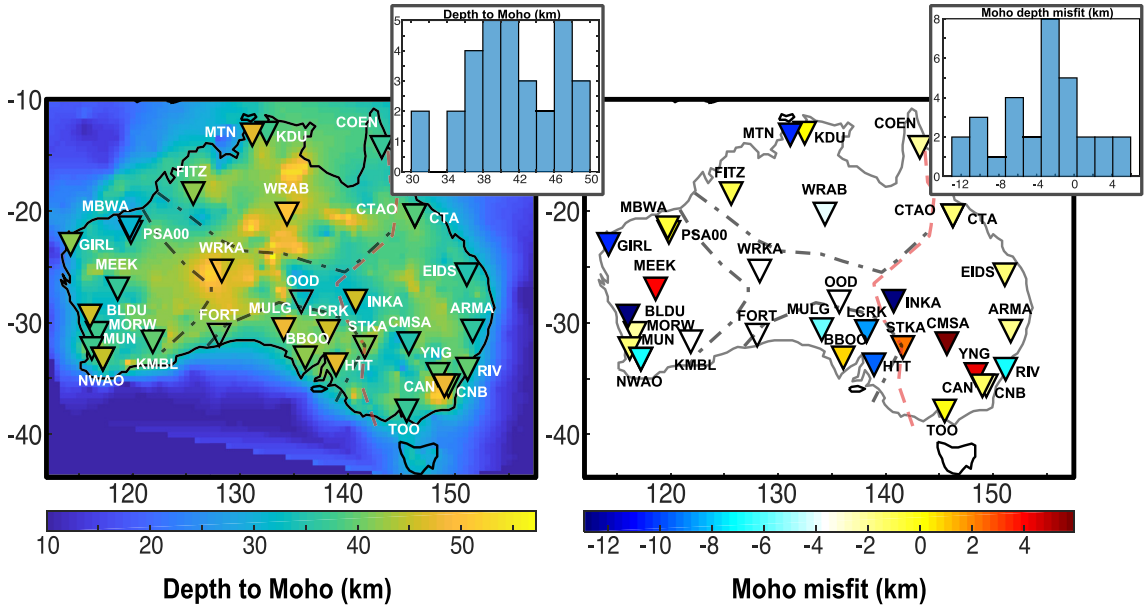

Figure 2. Depth to Moho as estimated from Ps receiver functions. (a) Depth in kilometers to Moho from our RFs plotted over the Moho depth as predicted by AuSREM (Kennett et al., 2012; Salmon et al., 2013). Inset shows histogram of Moho depth values. (b) Misfit between our Moho pick and that estimated by AuSREM, in kilometers. Inset shows histogram of misfit values. AuSREM, Australian Seismological Reference Model; RF, receiver function.

the Moho when compared to our results. Overall, this indicates that AuSREM is a robust model that agrees well with our Ps results.

Most stations showed relatively good agreement between the depth of the Moho as estimated by Sp and Ps (see Figure S1). However, there were some noticeable outliers. At station CNB, Ps receiver functions predict a deeper Moho than Sp by almost 10 km; additionally, neither estimate falls within the error bars of the other. INKA had a similar noticeable discrepancy, with nearly 20 km between Moho estimates. CAN too has a large gap between the Ps estimate and the Sp estimate, with a much deeper Ps estimate. MUN and PSA00 also had discrepancies between the Ps and Sp estimate, but in these cases the Ps estimate was shallower than the Sp estimate. At all other stations, the estimates from the two methods fell within one another's error bars or were very close. When there are discrepancies between the two methods in the estimated depth to the Moho, we defer to the results of the Ps receiver functions because they are better able to resolve structure at Moho depths due to their higher frequency content. The Moho depths for both Ps and Sp are reported in Tables 1–3.

3.2. Quality Control and Phase Picking of Sp Receiver Functions

Sp receiver functions were calculated for 88 stations across the Australian continent. However, limited data availability and/or quality ultimately restricted the total number of stations used in our subsequent analysis of mantle structure to 34 stations (Figure 3). RF quality was rated as good, fair or poor. For a station to be rated fair or good more than 50 events were required, as stations with fewer events typically yielded RFs that appeared unstable (rapid, large amplitude oscillations). Other metrics used in determining RF quality included the presence of a well-defined positive phase found at depths similar to the estimated Moho and relatively small error bars (an admittedly subjective criteria). Supplementary Figure 2 includes all of the Sp receiver functions calculated, including those which were rated as poor and not included in our analysis of lithospheric structure.

In this study, as in Ford et al. (2010), the criteria for the selection of a negative phase within a RF is a critical first step in determining the type of structure the negative phase(s) might represent. To begin, negative phases can only be selected if they fall between the positive phase inferred to be the Moho (magenta lines in Figure S2), down to a depth corresponding to the base of the negative velocity gradient determined from

Table 1
Results of Sp and Ps Receiver Function Analysis: Moho depths

Network	Station	Latitude	Longitude	Index	Total time	# Of waveforms	Moho: Sp (km)	Moho: Ps (km)	Rank (P/F/G)	Vs profile cluster
AU	ARMA	−30.418	151.629	1	15	339	32	36	G	1
AU	BBOO	−32.810	136.059	2	15	275	43	42	G	5
AU	BLDU	−30.615	116.709	3	16	330	39/56	38	G/F	2
AU	CMSA	−31.538	145.692	4	18	240	30	35	G	2
AU	CNB	−35.315	149.363	5	16	217	32	41	G	1
AU	COEN	−13.957	143.175	6	16	225	37	37	G	1
AU	CTA	−20.088	146.250	7	25	184	35	39	G	1
AU	EIDS	−25.369	151.082	8	16	382	35	35	G	1
AU	FITZ	−18.098	125.640	9	25	222	29/46	42	F	4
AU	FORT	−30.779	128.059	10	27	229	46	–	F	3
AU	GIRL	−22.643	114.234	11	24	245	43	42	G	2
AU	HTT	−33.431	138.922	12	10	57	46	47	G	7
AU	INKA	−27.741	140.746	13	6	70	28	46	F	6
AU	KDU	−12.687	132.473	14	11	69	40	38	G	4
AU	KMBL	−31.367	121.882	15	19	257	44	40	G	3
AU	LCRK	−30.447	138.216	16	6	85	46	46	G/F	6
AU	LHI	−31.520	159.061	17	12	232	25	–	G	1
AU	MEEK	−26.638	118.615	18	16	205	41	37	G	2
AU	MORW	−29.068	116.040	19	16	301	44	46	G	2
AU	MTN	−12.844	131.133	20	13	124	33/45	47	G/F	5
AU	MULG	−30.282	134.059	21	6	86	50	48	G	4
AU	MUN	−31.978	116.208	22	18	279	47	38	G	2
AU	NWAO	−32.928	117.239	23	25	155	40	45	G	2
AU	OOD	−27.794	135.688	24	6	80	48	–	G/F	3
AU	PSA00	−21.573	119.846	25	8	177	28/47	30	G	2
AU	RIV	−33.829	151.158	26	15	74	27	40	G	1
AU	STKA	−31.876	141.596	27	25	302	41	41	G	4
AU	TOO	−37.571	145.491	28	16	255	30	37	G	1
AU	WRKA	−25.038	128.296	29	10	157	48	–	G	3
AU	YNG	−34.298	148.396	30	20	288	33	40	G	1
G	CAN	−35.319	148.996	31	32	523	29	48	G	1
II	WRAB	−19.934	134.360	32	25	313	42	50	G	6
IU	CTAO	−20.088	146.255	33	28	530	38	39	G	1
IU	MBWA	−21.159	119.731	34	18	465	29/49	31	F	2
IU	NWAO	−32.928	117.239	35	28	610	43	45	G	2

AuSREM plus an additional 25 km to account for uncertainty in the negative velocity gradient depth. This uncertainty range has been chosen based on the interpolated model spacing from the mantle component of AuSREM (Kennett et al., 2012). From there, we designate significant negative phases to be up to the two largest negative amplitude phases, as taken from the mean amplitude of the single-binned Sp receiver function (Figure 3 and Figure S2). The largest negative phase, designated "negative Phase 1" in later discussion and selected for at every Good/Fair station, is the largest negative phase present. It is represented as a solid black, horizontal line at each station in Figure 3. If another, negative phase of comparable amplitude

Table 2
Results of Sp and Ps Receiver Function Analysis: Negative Phase 1

Network	Station	Ford 2010	Ford 2010 HVLid	Ford 2010 LAB/MLD	NVG	LAB/MLD	Negative Phase 1	2Sigma(D)	2Sigma(D)	Amplitude	2Sigma(A)	2Sigma(A)
AU	ARMA	93 ± 16	<150	LAB	<150	LAB	**74**	67	80	−0.0048	−0.0058	−0.0037
AU	BBOO	131 ± 9	150–175	LAB	Absent	MLD	**70**	64	75	−0.0038	−0.0051	−0.0025
AU	BLDU	–	–		100–175	MLD/both	**77**	73	82	−0.0075	−0.0087	−0.0063
AU	CMSA				<175	LAB	**78**	72	84	−0.0078	−0.0094	−0.0062
AU	CNB				<125	LAB	**80**	75	88	−0.0056	−0.0074	−0.0038
AU	COEN	67 ± 8	Absent	LAB	<100	LAB	**85**	80	91	−0.0073	−0.0088	−0.0058
AU	CTA				<125	LAB	**76**	71	81	−0.0063	−0.0076	−0.0051
AU	EIDS	76 ± 12	<150	LAB	<125	LAB	**76**	73	80	−0.0070	−0.0080	−0.0060
AU	FITZ	81 ± 8	125–225	MLD	125–175	MLD/both	**77**	68	84	−0.0055	−0.0066	−0.0045
AU	FORT	79 ± 6	125–200	MLD	125–225	MLD/both	**80**	75	85	−0.0031	−0.0044	−0.0018
AU	GIRL				75–175	MLD	**68**	62	72	−0.0045	−0.0055	−0.0036
AU	HTT				50–175?	LAB	**85**	78	90	−0.0084	−0.0110	−0.0059
AU	INKA				Absent	MLD	**61**	54	67	−0.0057	−0.0074	−0.0041
AU	KDU				125–175	MLD/both	**80**	68	87	−0.0073	−0.0945	−0.0052
AU	KMBL	85 ± 14	125–225	MLD	125–225	MLD	**79**	72	85	−0.0041	−0.0053	−0.0042
AU	LCRK				Absent	MLD	**118**	113	124	−0.0061	−0.0078	−0.0044
AU	LHI				<150	LAB	**82**	78	85	−0.0061	−0.0076	−0.0046
AU	MEEK				100–225	MLD/both	**79**	72	85	−0.0072	−0.0088	−0.0056
AU	MORW				100–175	MLD/both	**78**	70	85	−0.0074	−0.0088	−0.0061
AU	MTN				Absent	MLD	**84**	60	89	−0.0058	−0.0072	−0.0044
AU	MULG				150–175	MLD	**75**	70	80	−0.0044	−0.0059	−0.0028
AU	MUN	–	–		75–150	Either	**76**	71	88	−0.0067	−0.0083	−0.0052
AU	NWAO				75–175	Either/both	**77**	70	82	−0.0052	−0.0070	−0.0033
AU	OOD				150–225	MLD	**97**	88	105	−0.0057	−0.0075	−0.0038
AU	PSA00				75–175	Both	**67**	61	86	−0.0077	−0.0097	−0.0057
AU	RIV				<150	LAB	**84**	79	89	−0.0067	−0.0097	−0.0037
AU	STKA	104 ± 9	100–175	LAB	125–175	MLD/both	**83**	77	87	−0.0041	−0.0053	−0.0029
AU	TOO	61 ± 11	Absent	LAB	<125	LAB	**70**	61	79	−0.0060	−0.0073	−0.0048
AU	WRKA				150–225	MLD/both	**74**	68	81	−0.0115	−0.0141	−0.0089
AU	YNG	70 ± 8	<150	LAB	<125	LAB	**81**	75	88	−0.0036	−0.0054	−0.0018
G	CAN				<125	LAB	**82**	77	88	−0.0052	−0.0063	−0.0040
II	WRAB	81 ± 14	175–200	MLD	Absent	MLD	**71**	66	78	−0.0041	−0.0053	−0.0029
IU	CTAO	73 ± 6	Absent	LAB	<125	LAB	**74**	71	78	−0.0092	−0.0102	−0.0081
IU	MBWA	69 ± 8	100–200	MLD	75–175	Either/both	**72**	67	78	−0.0050	−0.0059	−0.0041
IU	NWAO	81 ± 8	100–175	MLD	75–175	Either/both	**77**	71	93	−0.0039	−0.0048	−0.0029

is present, it is called the "negative Phase 2," and is marked with a solid gray, horizontal line in Figure 3. Three things should be noted with these designations, the first is that we assume nothing about either phase in terms of their physical properties or what sort of boundary they represent. Both represent a decrease in velocity with increasing depth somewhere within the mantle. Both could be located within the potential LAB depth range or both could be located at depths associated with the lithospheric mantle, or they could each represent a different structure. We endeavor to define boundaries associated with the negative phases in Section 3.4. The second is that while negative Phase 1 is typically shallower than negative Phase 2, this is

Table 3
Results of Sp and Ps Receiver Function Analysis: Negative Phase 2 and Others

Network	Station	Negative Phase 2	2Sigma(D)	2Sigma(D)	Amplitude	2Sigma(A)	2Sigma(A)	Other (>0.001)	Other (>0.001)
AU	ARMA	**93**	60	104	−0.0025	−0.0035	−0.0016	NaN	NaN
AU	BBOO	**199**	193	204	−0.0050	−0.0034	−0.0018	96	NaN
AU	BLDU	**193**	186	198	−0.0024	−0.0036	−0.0012	NaN	NaN
AU	CMSA	**127**	119	136	−0.0028	−0.0039	−0.0017	188	NaN
AU	CNB	**117**	110	122	−0.0034	−0.0050	−0.0017	NaN	NaN
AU	COEN	**66**	60	103	−0.0027	−0.0039	−0.0015	163	NaN
AU	CTA	**109**	104	115	−0.0043	−0.0057	−0.0031	NaN	NaN
AU	EIDS	**NaN**	NaN	NaN	NaN	NaN	NaN	NaN	NaN
AU	FITZ	**122**	112	134	−0.0026	−0.0035	−0.0016	NaN	NaN
AU	FORT	**216**	213	220	−0.0037	−0.0049	−0.0024	NaN	NaN
AU	GIRL	**NaN**	NaN	NaN	NaN	NaN	NaN	NaN	NaN
AU	HTT	**NaN**	NaN	NaN	NaN	NaN	NaN	NaN	NaN
AU	INKA	**101**	97	107	−0.0046	−0.0061	−0.0031	287	NaN
AU	KDU	**99**	60	111	−0.0037	−0.0063	−0.0012	NaN	NaN
AU	KMBL	**113**	104	120	−0.0032	−0.0045	−0.0195	249	NaN
AU	LCRK	**67**	60	73	−0.0047	−0.0069	−0.0026	271	NaN
AU	LHI	**101**	96	105	−0.0030	−0.0044	−0.0015	56	186
AU	MEEK	**129**	124	134	−0.0051	−0.0066	−0.0036	NaN	NaN
AU	MORW	**190**	177	196	−0.0028	−0.0043	−0.0012	NaN	NaN
AU	MTN	**64**	59	90	−0.0053	−0.0065	−0.0040	170	***225***
AU	MULG	**109**	113	103	−0.0028	−0.0041	−0.0015	169	NaN
AU	MUN	**NaN**	NaN	NaN	NaN	NaN	NaN	NaN	NaN
AU	NWAO	**109**	105	114	−0.0030	−0.0046	−0.0014	186	NaN
AU	OOD	**NaN**	NaN	NaN	NaN	NaN	NaN	NaN	NaN
AU	PSA00	**81**	61	87	−0.0073	−0.0091	−0.0056	120	170
AU	RIV	**153**	149	157	−0.0047	−0.0072	−0.0022	69	NaN
AU	STKA	**137**	114	143	−0.0021	−0.0032	−0.0010	NaN	NaN
AU	TOO	**NaN**	NaN	NaN	NaN	NaN	NaN	NaN	NaN
AU	WRKA	**222**	189	228	−0.0030	−0.0050	−0.0011	NaN	NaN
AU	YNG	**128**	123	133	−0.0035	−0.0048	−0.0022	NaN	NaN
G	CAN	**188**	182	194	−0.0029	−0.0041	−0.0017	50	NaN
II	WRAB	**91**	63	97	−0.0030	−0.0042	−0.0019	135	198
IU	CTAO	**118**	107	124	−0.0019	−0.0027	−0.0011	NaN	NaN
IU	MBWA	**87**	63	93	−0.0033	−0.0044	−0.0023	NaN	NaN
IU	NWAO	**132**	128	137	−0.0027	−0.0037	−0.0018	NaN	NaN

not universally true (see stations FORT and LCRK in Figure 2 or Tables 1–3). The third is that the decision to select one versus two negative phases at a given station is subjective and varies from station to station. Not all stations have a second phase selected. In contrast to Ford et al. (2010), we have chosen to select more than one phase due to the fact that many stations have multiple negative phases that appear to be well resolved. Our intention in selecting the two largest phases is to more completely describe the mantle structure present beneath Australia. The depth and amplitude of these negative phases, along with their associated uncertainties, are included in Tables 1–3. In Figure 3 (dashed gray lines) and Tables 1–3, we also include information on up to two smaller negative phases. However, these negative phases are not directly compared

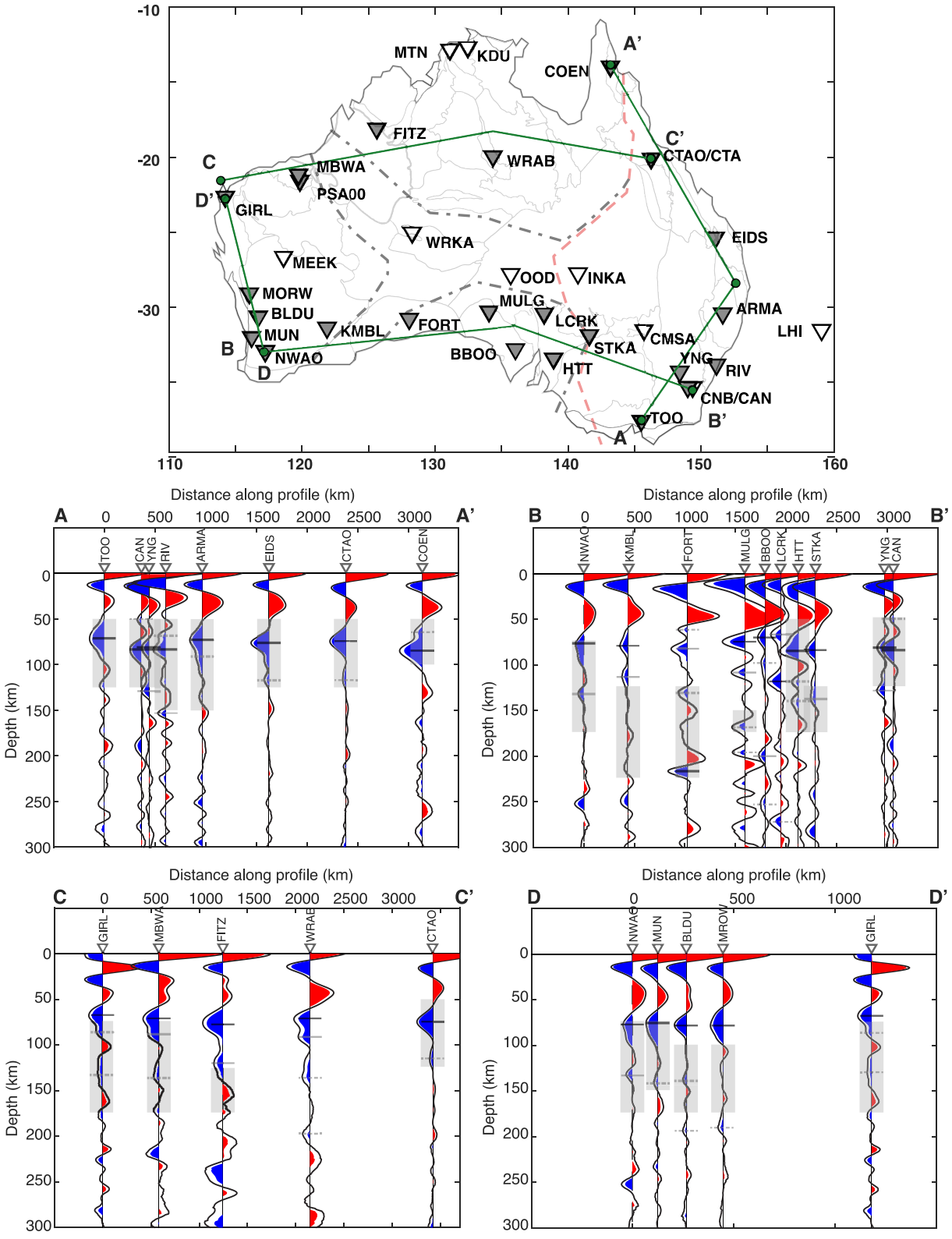
-10
-20
-30
110
120
130
140
150
160
MTN
KDU
COEN
A'
FITZ
C'
CTAO/CTA
C
MBWA
WRAB
PSA00
D'
GIRL
WRKA
EIDS
MEEK
OOD
INKA
MORW
MULG
ARMA
BLDU
LCRK
KMBL
FORT
MUN
CMSA
LHI
B
STKA
NWAO
BBOO
YNG
HTT
RIV
D
CNB/CAN
TOO
B'
A
Distance along profile (km)
A
A'
TOO
CAN
YNG
RIV
ARMA
EIDS
CTAO
COEN
Depth (km)
B
B'
NWAO
KMBL
FORT
MULG
BBOO
LCRK
HTT
STKA
YNG
CAN
C
C'
GIRL
MBWA
FITZ
WRAB
CTAO
D
D'
NWAO
MUN
BLDU
MROW
GIRL

to the AuSREM model in later discussion (Section 3.4). We acknowledge that while it is possible to pick and analyze every negative phase that is statistically well resolved (i.e., negative phase energy exceeding zero when including two sigma confidence limits), the goal of this study is to focus on the largest amplitude/most significant phases in order to place first order constraints on mantle structure beneath Australia.

3.3. Negative Phase Depths Across Australia From Sp Receiver Functions

As described above, our analysis is restricted to up to the two largest, most robustly imaged negative phases present at each station labeled good or fair. The collectively averaged depth of these phases is 94 km and the median depth is 81 km, and the average depth to the largest negative phase (referred to earlier as negative Phase 1) at each station is 83 km, with a median depth of 78 km. Eighty-eight percent of negative Phase 1 phases fall within 15 km of the negative Phase 1 average (83 km), while only 33% of all negative phases fall within the average of all negative phases (94 km). This observation indicates that while the largest negative phases (negative Phase 1) tend to cluster at a single depth, negative Phase 2 is significantly more distributed. This is also demonstrated in Figure 4.

There appears to be no systematic variation between negative phase depth and tectonic age in Australia although there does appear to be some consistency regionally. For example, in Figure 5a stations located within/near the Yilgarn Craton (i.e., MEEK, MORW, BLDU, MUN, NWAO, and KMBL) have their negative Phase 1 located within a very consistent depth range of 74–79 km. This is also demonstrated in profile DD′ in Figure 3. This remarkable consistency is not observed everywhere, as variations in depth in most regions tend to be greater than 5 km, although regional trends are still apparent, such as on the eastern margin of Australia (profile AA′ in Figure 3).

The average amplitude of negative Phase 1 is −0.006 and there appears to be no correlation between tectonic age and amplitude, although some weak correlations between regional location and amplitude may exist as stations colocated near each other appear to have similar amplitudes (with exceptions) (Figure 5). The average amplitude of negative Phase 2 is −0.0036, which is roughly half the amplitude of the average of negative Phase 1 amplitudes. In the following sections, we carefully consider variations in the depth and amplitude of both negative phases as they compare to the previously published work of Ford et al. (2010) as well as how they relate to the AuSREM mantle model.

3.4. Comparison to Previously Published Sp Receiver Function Results

This study is an update to Ford et al. (2010), calculated using a similar method with slight variations to our own (see Section 2.2 for more information). Ford et al. (2010) used the negative velocity gradient inferred from surface wave tomography (Fischwick et al., 2008) to define the potential lithosphere-boundary range at each station. We use a similar definition, but utilize the AuSREM mantle velocity model (Kennett et al., 2012). Beyond differences in velocity model used, the process to determine whether the negative phase represents a conversion at the LAB or a discontinuity within the lithosphere (MLD) is the same. At each station, a 1-D velocity profile is obtained from AuSREM. The depth range of the negative velocity gradient is recorded at the location (see Tables 1–3), as well as shown as a gray box in Figure 3 and in Figure S2. The 1-D profile for each station is shown in Figure 9. If negative Phase 1 or 2 falls within the range of the negative velocity gradient, then it is interpreted to potentially be a conversion at or within the LAB. If the negative phase is observed to be shallower than the negative velocity gradient, then it is interpreted to be an MLD. Due to the fact that we are picking the two largest negative phases at some stations, you will notice in

Figure 3. (top) Map of the 34 good and fair stations (inverted triangles) used in this study. Gray filled in stations have RF results plotted in cross section. Remaining stations are shown in Figure S2. Green lines show cross section locations. (middle and bottom rows) Cross sections A–A′, B–B′, C–C′, and D–D′. Station stacked Sp receiver functions are plotted for individual stations along cross section lines. Red phases correspond to a velocity increase with depth and blue phases correspond to a velocity decrease with depth. The black line corresponding to the mean of the bootstrapped RFs is plotted, and only the statistically significant portions of the positive and negative phases are shown. Negative phase picks are plotted as black horizontal lines (negative Phase 1), gray horizontal lines (negative Phase 2), and other negative phases of potential interest are highlighted with dashed gray horizontal lines. Gray, semitransparent boxes illustrate the depth range of the negative velocity gradient determined from the AuSREM velocity model. AuSREM, Australian Seismological Reference Model; RF, receiver function.

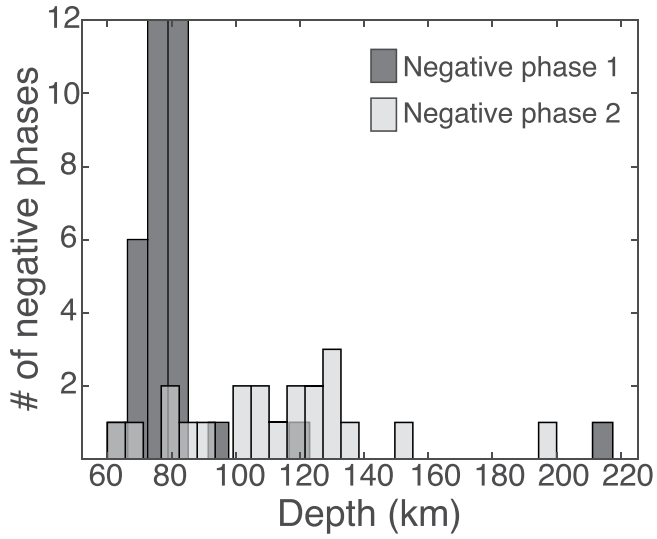

Figure 4. Histogram of depth distribution of negative Phase 1 and negative Phase 2 for all stations. Note that most of negative Phase 1 picks fall between 60 and 120 km.

Tables 1–3 that some stations have both an LAB phase as well as an MLD phase listed ("Both" in Tables 1–3). If a negative phase falls on the cusp of the negative velocity gradient, but has overlapping error bars, we denote that it could be "Either," meaning that the interpretation is not clear. We report our results regionally, starting with the Tasmanides, then the NAC, SAC, and WAC.

3.4.1. Phanerozoic Australia

In eastern Australia at stations CTAO (within 1 km) and TOO (within 9 km), our results fall within error of the originally published work of Ford et al. (2010). At YNG, the fit is slightly poorer, with a misfit of 11 km, however, even then the error bars from the two studies do overlap. The same overlapping error is also true for stations ARMA, however, upon closer inspection of RFs it has a small but well constrained pulse of negative phase energy next to the largest negative phase (Figure 3) that agrees within 1 km of the originally reported results of Ford et al. (2010). In Phanerozoic Australia, the stations ARMA, EIDS, TOO, YNG, RIV, CNB, CMSA, and CTAO all have negative phases that clearly fall within the negative velocity gradient inferred from AuSREM. The negative phases at these stations are thought to represent a conversion at or within the LAB, in agreement with Ford et al. (2010). At most of these stations, the negative velocity gradient falls within ±25 km the same range reported in Ford et al. (2010). Exceptions to this include stations CTAO and TOO, which had no reported negative velocity gradient in Ford et al. (2010) likely due to the fact that the gradient was shallower than what was resolvable. At station INKA (within the Thomson Orogen), there is no negative velocity gradient at lithospheric depths, and thus we interpret the negative phase at 61 km to be an MLD.

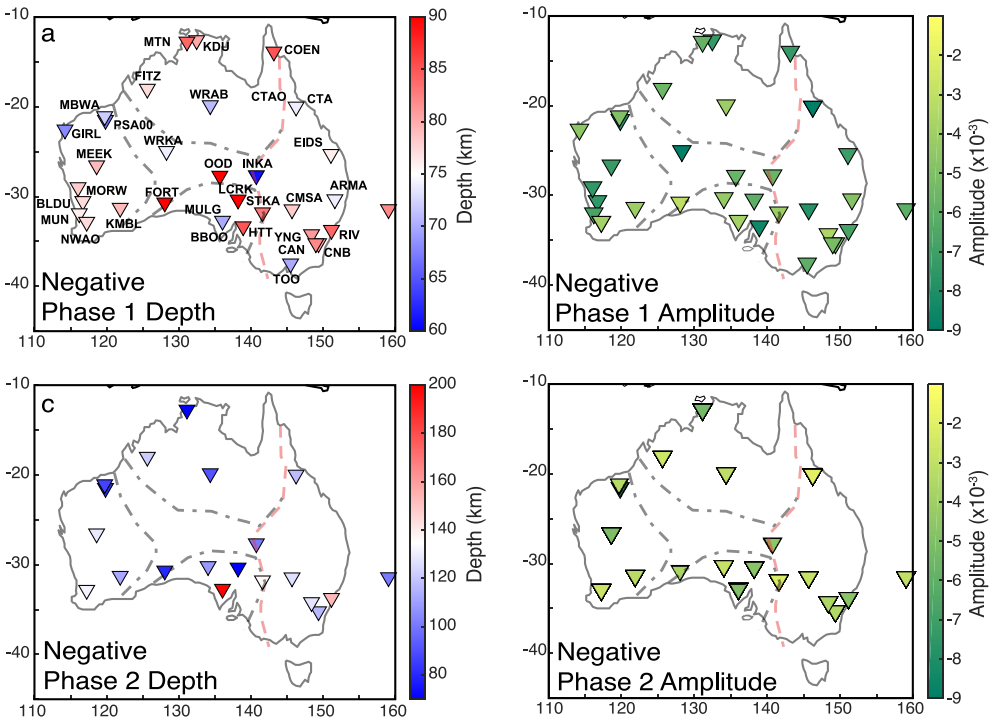

Figure 5. (a and c) Depth to (a) negative Phase 1 and (c) negative Phase 2, in kilometers. (b and d) Amplitude of (b) negative Phase 1 and (d) negative Phase 2. Outlines show cratons and Tasman Line.

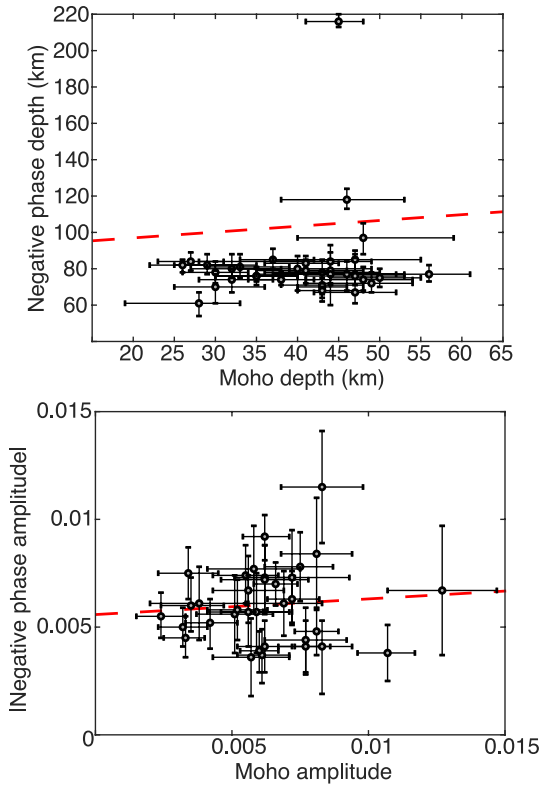

Figure 6. Scatter plots (including error bars) of relationship between negative phase depth and Sp Moho depth and negative phase amplitude and Sp Moho amplitude.

Ford et al. (2010) observed a distinct variation in amplitude correlated with depth at the stations where they found an LAB phase (mostly along the eastern margin of the continent). While we cannot directly compare our results (due to normalization and deconvolution differences), we can compare possible trends in our new results to the old ones. As discussed above, we observed relatively modest variations in amplitude between stations, and no correlation with tectonic age is seen (Figures 5b and 5d). Using best fitting models of the receiver function amplitude, locations of recent volcanism, and inferred topography of the LAB, Ford et al. (2010) postulated that either mantle melting influenced lithospheric thickness or that melt focused in regions of thinner lithosphere. In Figure 7, we plot our results including those at stations BBOO and STKA: though we do not observe the LAB at BBOO, we want to compare the trend to Ford et al. (2010). We observe a weak correlation between negative phase depth and amplitude for stations YNG, ARMA, TOO, and to a lesser degree EIDS and CTAO (Figure 7). However, BBOO and STKA again prove problematic and when new stations from this study are added, the correlation appears to break down completely (Figure 7). This discrepancy indicates that the apparent correlation observed in Ford et al. (2010) was the result of sampling bias and presents a clear argument for why densification of permanent networks is critical for improving our understanding of lithospheric structure.

3.4.2. North Australian Craton

In the NAC at stations FITZ and WRAB, the largest negative phase (negative Phase 1) falls within error of the Ford et al. (2010) study. At FITZ, our results are within 5 km of the originally recorded negative phase depths of Ford et al. (2010). At COEN, there is a slight discrepancy, with our negative phase falling a few kilometers deeper than that in Ford et al. (2010), even once error bars are considered. The largest negative phase at WRAB is located 10 km shallower than the negative phase reported in Ford et al. (2010) but again falls within the ±14 km of uncertainty. It is possible that the small changes in negative phase depth are due to the difference in velocity model used in the migration. Abt et al. (2010) migrated Sp receiver functions using AK135 as well as more regionally accurate Vp and Vs models and found that depths changed by no more than 6 km. It is likely that the newer values reported are more accurate since the original migration model used in Ford et al. (2010) was the globally averaged, 1-D model AK135, whereas the AuSREM model used in this study is specific to Australia. Another key difference between this study and Ford et al. (2010) is that we also report the negative phase depths for additional phases. This does not mean that those additional phases were not present in the original study. For example, in this study at station WRAB, the largest negative phase (negative Phase 1) is located at a depth of 71 km, while a second significant negative phase (negative Phase 2) is found at 91 km, and two additional negative phases are observed at 135 and 198 km. Upon comparison to the plotted Sp receiver function in Figure 6d (Ford et al., 2010), it is clear that an additional phase is located at ~140 km, which agrees with our observations. At stations FITZ, KDU, MTN, and WRAB we observe negative pulses that fall above the negative velocity gradient interpreted from AuSREM; at MTN and WRAB, we observe multiple MLDs. However, at FITZ and KDU, we observe a shallower MLD and a deeper negative phase that does correspond to the negative gradient in AuSREM, thus we interpret these as the LAB. WRKA (which is not strictly within the NAC but adjacent), also has these double negative phases interpreted as an MLD and the LAB. At COEN, on the eastern edge of the NAC, our negative Phase 1 fell within the depth range of the negative gradient and thus is likely the LAB.

3.4.3. South Australian Craton

Results at FORT are in good agreement with Ford et al. (2010), with our negative Phase 1 at 80 km and their largest phase at 79 km. As with their study, we interpret this energy to be an MLD. However, we do observe energy at greater depths that we interpret as the LAB. At STKA, we report negative phase energy at

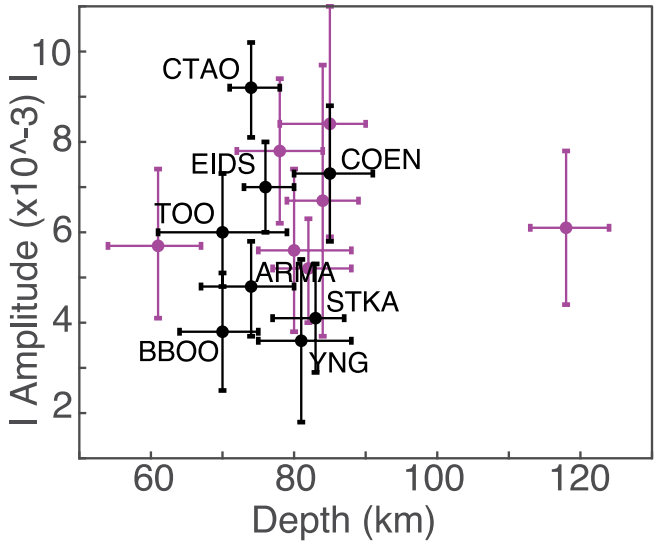

Figure 7. Plot of negative Phase 1 amplitude versus phase depth for stations in Phanerozoic Australia. Ford et al. (2010) posited a negative correlation between the two. However, with increased station coverage, this does not appear to be the case. Black symbols correspond to Phanerozoic station results included in both the original (2010) study and this study. Magenta symbols are for stations new this study.

83 (−6/+4) km (negative Phase 1) and 137 (−23/+6) km (negative Phase 2), whereas Ford et al. (2010) report a depth of 104 ± 9 km. At BBOO negative energy is present at depths of 70 (−6/+5) km (negative Phase 1) and 199 (−6/+5) km (negative Phase 2), as well as a small amount of negative phase energy at 96 and 251 km. In the study by Ford et al. (2010), the negative phase depth is reported to be at 131±9 km and was interpreted as the LAB. However, there is no negative velocity gradient on the AuSREM profile, thus we have interpreted the largest negative phase to be an MLD. At station OOD (just to the north of the SAC), we also observed a negative phase within the lithosphere that we interpreted as an MLD. However, at stations LCRK and MULG, we observed multiple negative phases within the negative velocity gradient of AuSREM, which we interpreted as being multiple MLDs. It should also be noted that LCRK had the largest negative Phase 1 depth of any station at 118 km. At station HTT, the negative phase at 85 km fell within the negative gradient of 50–175 km, thus this phase is the LAB. STKA (in the Curnamona Province) was reported by Ford et al. (2010) to have an LAB: this study found a negative conversion both within the lithosphere and within the negative velocity gradient, indicating the presence of an MLD and the LAB.

3.4.4. West Australian Craton

In the WAC, KMBL, MBWA, and NWAO have results within error of Ford et al. (2010). At MBWA and NWAO, negative phases at both stations are within ±5 km of those reported in Ford et al. (2010). However, the depth range of the negative velocity gradients at both stations has shifted to shallower depths, bringing the potential LAB depth range within error of the negative phases at both stations. At NWAO, negative phases 1 and 2 are interpreted to be the result of conversions within the LAB depth range, although the shallower phase has error bars that extended to lithospheric depths. While at MBWA the shallower of the two phases falls within the lithosphere, its lower error bar extends into the negative velocity gradient. These results indicate that while the fundamental observations (depth of negative phases) have remained the same, the interpretation has changed as the result of a different velocity model. At KMBL, the largest negative phase is 6 km shallower than originally estimated but well within the ±14 km of uncertainty in the originally reported study. This phase is interpreted to be an MLD. As at MBWA, both negative phases at PSA00 and MUN were ambiguous and fell within error of the LAB depth range. At BLDU, MORW, and MEEK, the shallower of the two phases fell within the lithosphere, while the deeper phase was either within the AuSREM negative gradient or within error it. Thus, we interpreted the shallower phases here to be MLDs and the deeper to be the LAB.

3.5. Determining Provenance of Negative Phases Using the AuSREM Velocity Model

We use AuSREM both to migrate results (translating a time series into a depth series) and to determine if the scattered phase is from the LAB or an MLD. If a negative phase falls within depths corresponding to an overall velocity increase within the AuSREM velocity model, it seems unlikely that what we are observing is a conversion at or within the LAB, as the seismic LAB is typically thought to be a region where velocities decrease. Instead, we assume that the negative phase falls within the lithospheric mantle and must represent a localized velocity decrease (MLD), capable of generating a large enough conversion to be visible in Sp receiver function results, but insufficient to be distinguished by lower resolution tomographic methods. The negative velocity gradients taken from the AuSREM velocity model are shown as gray boxes in Figure 3 and Figure S2.

To aid us in our discussion, the velocity profiles for the stations analyzed in this study are clustered according to profile shape. The station clusters are shown in Figure 8 and are plotted on top of absolute Vs at a depth of 150 km (from AuSREM). In Figure 9, the velocity profiles (and corresponding phase depths) for each cluster of stations are shown down to a depth of 300 km, including an average (in red). For the remainder of

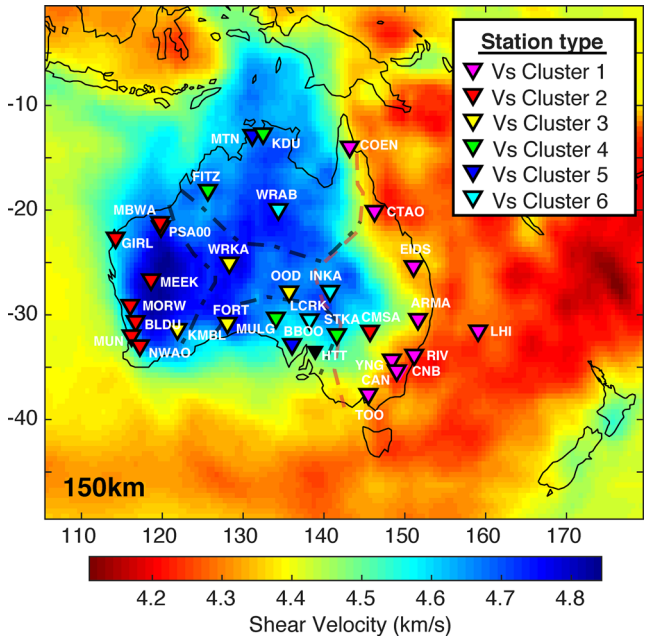

Figure 8. Base map is absolute shear velocity taken at 150 km from AuSREM. Stations are labeled by Vs cluster, see Figure 9 and text for more information. Vs Cluster 1, shown in Figure 9, consists of velocity profiles that exhibit no high velocity lid. Outlines shown for cratons and the Tasman Line. AuSREM, Australian Seismological Reference Model.

this section, we review the key characteristics of each Vs profile cluster in terms of profile shape, relative geographic location, and whether negative phases within the cluster are typically MLDs or the LAB.

Profiles in Vs Cluster 1 (shown in Figure 9) exhibit no high velocity lid. Negative velocity gradients are typically present from 50 to 150 km, with the greatest drop in velocity at depths of 50–100 km, consistent with a shallow LAB. Stations within Vs Cluster 1 are indicated in Tables 1–3 and Figure 8 and are exclusively found on the continent's eastern margin or in one case, on Lord Howe Island, an ocean island station east of the continent. We note that while COEN is west of the Tasman Line and on rock of Proterozoic age, it has an LAB phase indicating that the lithosphere in this region has been removed or has properties more similar to lithosphere located east of the Tasman Line. In all cases, absolute velocities are low (<4.5 km/s) at 150 km (Figure 8). Negative Phase 1 and negative Phase 2 for stations in Vs Cluster 1 are clearly separated, with the largest negative phases found between 70 and 85 km and the secondary negative phase found at between 101 and 153 km. Given that the depth range for the largest negative phases are within the same range as where the largest drop in velocity is found (50–100 km), we believe these negative phases originate from scattering at the LAB. This is in good agreement Ford et al. (2010), where eastern margin station RFs were thought to have negative phases originating from the LAB. The origin of the deeper negative phases is less clear. Since negative velocity gradients are present to 150 km at most stations, it is possible that the LAB should be thought of as more of a transition and both phases are part of a more complex, less continuous progression of lithospheric mantle to asthenosphere. Alternatively, the negative phases at greater depths may be a boundary in melting within the asthenosphere. Electrical conductivity is often linked to the presence of melt, and there is a region of increased conductivity beneath Phanerozoic Australia between at least 92 and 172 km (B. Kennett et al., 2018; L. Wang et al., 2014). Additionally, electrical conductivity in the asthenosphere may be linked to the presence of small amounts of carbonate melt and Phanerozoic volcanism, decreasing seismic velocity (Aulbach, Massuyeau, & Gaillard, 2017; Davies et al., 2015; Gaillard et al., 2008).

The key characteristic of velocity profiles in Vs Cluster 2 is that on average they have increasing velocities to 75 km and then decreasing velocities from 75 km to, on average, 175 km. This suggests a thin, high velocity lid, with a clear transition to a low-velocity asthenosphere. The majority of the stations (all but one) are located in WAC. However, station CMSA, which is located within Phanerozoic Australia is an outlier in terms of location (but not with respect to the velocity profile cluster itself). The largest and second largest phases at stations within Vs Cluster 2 are not as clearly separated in Vs Cluster 1, however, the largest negative phases are typically located at shallower depths than the smaller amplitude negative phases. For the deeper, typically smaller phases, the depths commonly correspond to the depth range of the negative velocity gradient, suggesting they are the result of scattering within the potential LAB depth range. Meanwhile, the average of the largest negative phases falls at a depth of 75 km, which marks the transition to a negative velocity gradient. At roughly half of the stations, the error bars extend the phase picks down to the corresponding negative velocity gradient for the given station, while for the other half the phase picks fall within the high velocity lithosphere. Choosing to abide by our definition of potential LAB versus MLD phases, this means that roughly half of the largest negative phases in Vs Cluster 2 are lithospheric in origin (MLD) while the other half are the result of scattering from within the transition from lithosphere to asthenosphere.

The average shear velocity profiles for Vs Clusters 3 and 4 have increasing velocities to 125 km. Below 125 km, velocities decrease in both averaged profiles, however, the local minimum in the averaged profile for Vs Cluster 3 is observed at 225 km, while the local minimum in the averaged profile for Vs Cluster 4 is seen at 175 km. Generally, the absolute changes in velocity for Vs Cluster 3 are larger, both within the high velocity lid, as well within the region of negative velocity gradient. In Vs Cluster 4, the decrease in velocity

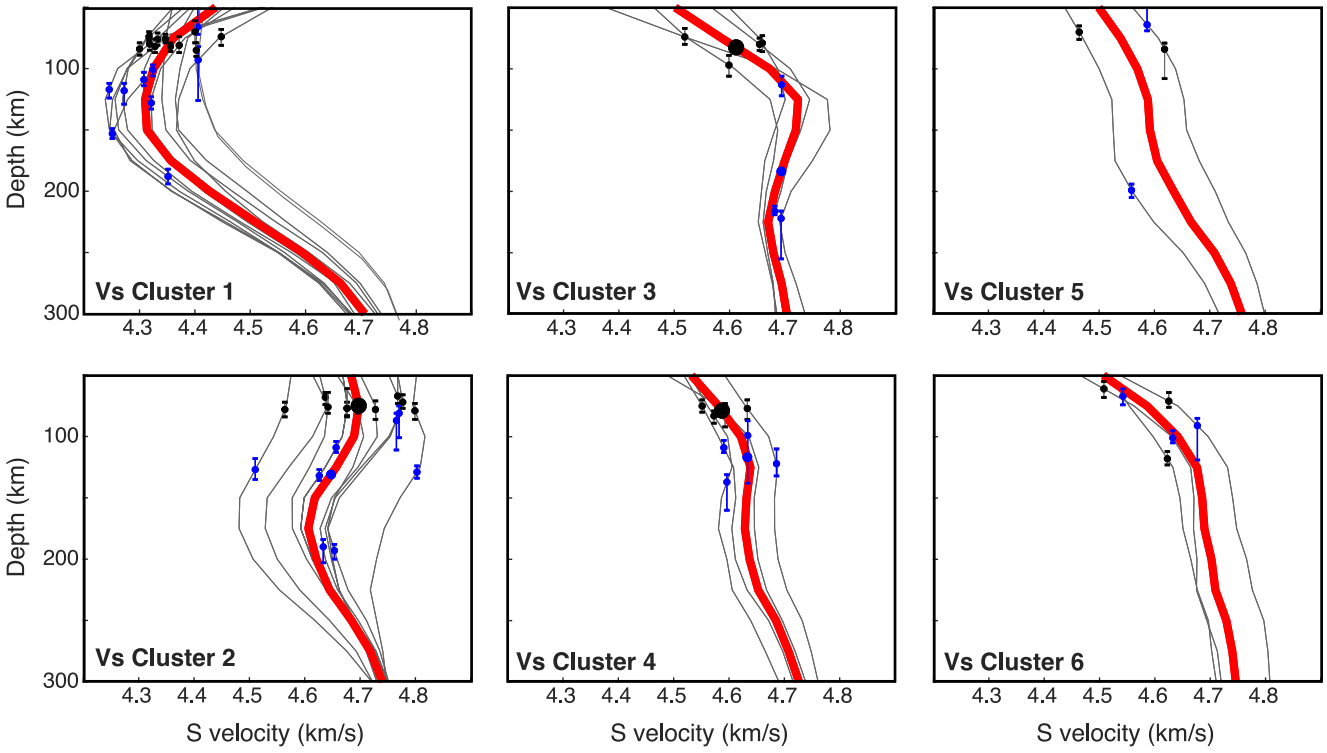

Figure 9. 1-D velocity profiles from the mantle shear velocity component of AuSREM. Red lines are the average velocity from that cluster of profiles. Small black dots with error bars are negative Phase 1 depths, and small blue dots are negative Phase 2 depths. See Figure 8 for geographic distribution of Vs clusters. AuSREM, Australian Seismological Reference Model.

within the negative velocity gradient is very small. Notably, the vast majority of the negative phases fall at depths above our defined potential LAB depth range indicating that at these stations the negative phases that we observed are predominately MLDs. The stations in Vs Clusters 3 and 4 are listed in Tables 1–3. In Figure 8, they are marked with the yellow and green inverted triangles and are located mostly in the NAC and SAC, with one in the WAC, and one slightly east of the Tasman Line. The stations are interspersed with stations labeled as belonging to Vs Clusters 5 and 6, which are marked as blue and cyan inverted triangles, respectively. The number of stations clustered as 5 and 6 are distinct from Vs Clusters 3 and 4, due to the fact that the stations in Vs Clusters 5 and 6 have no apparent negative velocity gradient, which suggests there is no observed seismic transition from lithosphere–asthenosphere to at least 300 km, suggesting a very gradual change from one to the other. Therefore, all of the negative phases at stations in these two clusters are MLDs.

4. Discussion

4.1. The Importance of Additional Stations

As mentioned in Section 2.1, this study has more stations and increased years of coverage from Ford et al. (2010), greatly improving the understanding of lithospheric complexity in Australia. However, coverage of the continent continues to expand, especially in more remote regions. Improved coverage with smaller station spacing would allow for the calculation of common-conversion point stacks, a method used to image lithospheric layering in the North American cratons (Chen et al., 2018; Hopper & Fischer, 2015, 2018; Hopper et al., 2014; Kind et al., 2017). This is particularly important because we have detected the presence of multiple MLDs at some stations (see Figure 10). Currently, we cannot say whether any of these structures are dipping as our RFs represent only the structure below the station/along the ray's path. Such information may provide evidence as to the origin of the MLDs, such as an ancient subduction zone setting as suggested by Hopper and Fischer (2015).

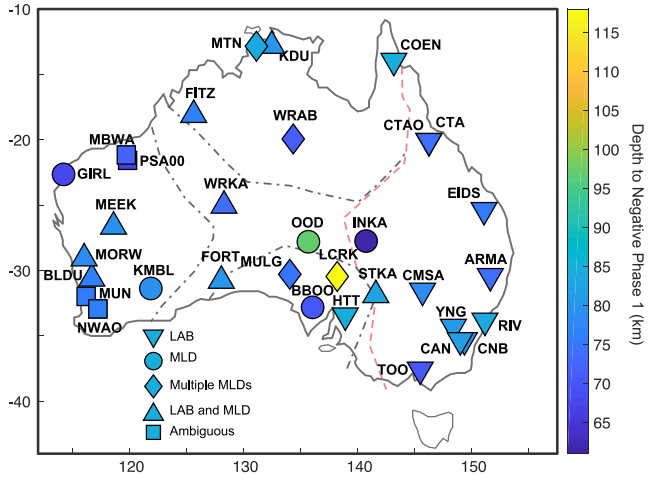

Figure 10. Depth to negative Phase 1 (km) and its interpretation. Stations plotted as inverted triangles only had an LAB, those as circles only had an MLD, diamond stations had multiple MLDs, normal triangles had both the LAB and MLD (labeled MLD/both in Table 2), and squares had phases that could be either the LAB or an MLD (labeled Either/Both in Table 2). LAB, lithosphere–asthenosphere boundary; MLD, midlithospheric discontinuity.

One important finding of Ford et al. (2010) was that at stations with an observable LAB there was a negative correlation between phase depth and amplitude (i.e., shallower phases had stronger amplitudes). The strongest, shallowest negative phases were observed in regions of recent volcanism. However, our study has found that with increased station coverage there does not seem to be a correlation (Figure 7). The previous negative correlation may have been an artifact of the limited station availability.

Additionally, Ford et al. (2010) did not report any observed LAB phases in western Australia. This study, however, reports four stations in the WAC at which the negative phase is interpreted to be the either and MLD or the LAB, and another three with both an MLD and the LAB. This is particularly interesting, as most of these stations fall within the Yilgarn and Pilbara cratons. These stations all belong to Vs Cluster 2, which contains a clear negative velocity gradient at 75–175 km depth, which is distinctly different from the velocity gradients at many of the other cratonic stations in Australia (see Vs Clusters 3–6 in Figure 9). The phases at these western stations all fall roughly between 70 and 90 km, which corresponds to the upper bound placed on the LAT by Yoshizawa and Kennett (2015). It is possible that there is a strong impedance contrast at the top of the LAT (such as the base of the chemical boundary layer; Lee et al., 2005), but that the lithosphere extends well below that depth and may be more mechanically coupled to the asthenosphere. Tomography has shown that the lithosphere in the southwestern portion of the Yilgarn craton may have been thinned (B. L. Kennett et al, 2013; Simons et al., 1999). However, the seven stations with observed and potential LAB span the entire Yilgarn craton, through the Capricorn Orogeny, and into the Pilbara craton, suggesting that localized lithospheric thinning cannot entirely explain the negative phases. For most stations, though, it seems likely that we may be observing the top of this LAT.

4.2. Comparisons to Seismic Reflectivity

A number of recent studies (Gorbatov et al., 2013; B. L. N. Kennett, 2015; B. L. N. Kennett & Furumura, 2016; B. L. N. Kennett & Sippl, 2018; Kennett et al., 2017; Sun & Kennett, 2016; Sun et al., 2018) have focused on a related seismic property, seismic wave reflectivity. Like RFs, this method can provide information about depth to discontinuities and layers, but unlike RFS the amplitude is not directly related to the impedance contrast between layers. These studies calculate *P* wave reflectivity through a method known as seismic daylight imaging and use a slightly higher and broader frequency band (0.5–4.0 Hz) than RFs (our Sp receiver functions are filtered at 0.03–0.5 Hz), useful for providing more detailed information on finer layering.

Multiple studies using this method have examined the structure of the Australian lithosphere in a way similar to RFs. B. L. N. Kennett (2015) first made use of this method to investigate lithosphere–asthenosphere reflectivity across Australia. That study used many of the same stations as this one but did not independently identify any phases in the midlithosphere. At stations STKA, YNG, EIDS, ARMA, YNG, and TOO, the MLD as identified by Ford et al. (2010) was at the top of the tomographically defined LAT of Yoshizawa (2014) and corresponds to some change in the frequency or character of reflectivity (B. L. N. Kennett, 2015; B. L. N. Kennett et al., 2017). MBWA and CTA both had MLDs that were at the base of a low frequency packet, while WRAB had an MLD within a higher frequency packet. Sun et al. (2018) investigated reflectivity in the WAC, and additionally interpreted their own phases within the midlithosphere. In general, they found a shallow MLD (~70–82 km), with the deepest phases in Proterozoic orogens. They reported an MLD at MEEK at ~65 km (we report one at 79 km), at KMBL at ~70 km (we report the most prominent phase at 79 km, but note another at 72 km), at PSA00 at ~60 km (we report the most prominent negative phase at 67 km, but do report another at 61 km), and at MBWA at ~70 km (we report one at 72 km). Sun et al. (2018) did note there was an 18 km discrepancy between the MLD they reported at KMBL and that reported by Ford et al. (2010),

which they explain as possibly being due to the presence of multiple MLDs, a possibility we confirm with this study. A study focusing on central Australia found similar results, with a marked change in the frequency content of *P* wave reflectivity profiles between 80 and 100 km (B. L. N. Kennett & Sippl, 2018). That study did not observe a clear, coherent midlithospheric phase in CCP stacks, but individual stations did show evidence of a possible discontinuity. Additionally, B. L. N. Kennett and Sippl (2018) did not observe any strong negative phases that they could associate with the LAB, a finding mirrored by our own results.

Other recent work has used this same method and combined it with others to investigate the nature of the lithosphere from a slightly different angle. B. L. N. Kennett and Furumura (2016) argued that the complex, high frequency coda observed for *P* and *S* waves from local earthquakes were a result of complex and multiscale velocity variations within the lithosphere. They argue that in addition to the first order changes in seismic velocity (such as those we observe), there may also be variations at much finer scales on the order of kilometers to tens of kilometers. MLDs may be a result of this fine-scale velocity variation. In reflection seismology, many reflectors arise due to such fine-scale variation, and the same effect may hold true for transmitted signals. The filtering of RFs may also have some effect on observations of MLDs. Most Sp receiver functions are filtered at relatively low frequencies (>0.5 Hz), which in turn results in less fine-scale variation in the results. This smoothing allows for velocity changes to be described in a few first order jumps, where in reality there may be more (B. L. N. Kennett et al., 2017). Multiscale heterogeneity may have implications for other properties of the lithosphere–asthenosphere system. It is linked to anisotropy (B. L. N. Kennett & Furumura, 2016; Yoshizawa, 2014; Yoshizawa & Kennett, 2015), changes in Mg# (Gaul et al., 2003; B. L. N. Kennett et al., 2017), and the top of the proposed LAT throughout Australia at ~70–100 km (Yoshizawa & Kennett, 2015). These properties are also linked to the MLD.

We cannot rule out the possibility that the MLDs we observe are due to multiscale heterogeneity, however, it should be noted that we do not currently have the observational data to support the idea that these variations in velocity at multiple scales exist everywhere. Additionally, while these variations may explain some of the observations we make regarding MLDs, the argument for multiscale heterogeneity relies on observations made in Australia. It may not explain MLDs that occur elsewhere in the world.

4.3. The Australian MLD and Lithospheric Layering

We observed negative phases interpreted to be MLDs at 17 stations, with 4 additional stations having ambiguous phases. These phases ranged in depth from 61 to 118 km, with most falling between 70 and 90 km. Most of these stations are located within Central Australia, either in the NAC, or in the Proterozoic orogens to its south suturing it together with the other Australian cratons. There are also MLD phases observed in the SAC, including the deepest observed at AU LCRK. Additionally, at 26 stations we observed a weaker negative phase either above or below their primary negative phase (i.e., the LAB or an MLD). This leads to the inference that there may be multiple MLDs at some stations; in particular we see evidence for layering in cratonic settings.

The presence of multiple lithospheric layers has been well documented in other cratons. Hopper and Fischer (2015) identified several discontinuities in the North American craton below the Moho at varying depths. The shallowest negative phase (~70–90 km) was interpreted to result from frozen-in volatile-rich melt. Below that were dipping negative phases (85–200 km) that may be the result of the formation or stabilization of the ancient lithosphere. Additionally, most cratonic stations used in the study could not identify a clear negative phase associated with the LAB, a finding mirrored in our own results. Sodoudi et al. (2013) observed two MLDs within the Kalahari craton, on at ~85 km depth that is most likely associated with a layer of anisotropy, and a second MLD between 150 and 200 km depth that seems to be linked to magmatic events and the base of the highly depleted cratonic lithosphere. In the stable western portion of the North China Craton, multiple MLDs are observed as well which may be linked to the evolution of the craton and multiple instances of melt infiltration throughout its history (Sun et al., 2020). Other studies have also indicated the presence of multiple phases beneath the Moho, both in cratonic and more active tectonic settings. Lekić and Fischer (2014) identified multiple negative phases in the oldest portions of the northwestern United States, with weaker amplitudes than those observed in the more tectonically active regions further to the west. This result is further strengthened by the presence of multiple MLDs to the east of the

Sevier thrust belt in the western United States, possibly explained by previous episodes of subduction (Ford et al., 2016; Hopper et al., 2014).

Just as Hopper and Fischer (2015) observed a consistent negative phase across terrane and age boundaries, we also observe a pervasive negative phase at almost every station between 70 and 100 km. Rychert and Shearer (2009) carried out a global Ps receiver function study and found a similar negative velocity drop in all settings at approximately the same depth range. The fact that almost all lithospheric types and tectonic settings seem to have this negative velocity drop has been used to argue for the presence of a global discontinuity at these depths. However, tomography seems to be insensitive to this boundary, as models often show fast, increasing velocities to at least 150 km and often deeper (B. L. Kennett et al., 2013; Schaeffer & Lebedev, 2013; Yoshizawa & Kennett, 2015). Other tomographic models have observed a velocity decrease at approximately the same depth as MLDs inferred from RF studies (Romanowicz, 2009; Yuan & Romanowicz, 2010). The one-dimensional shear velocity profiles from AuSREM we used to determine the provenance of negative phases lacked a negative velocity gradient at depths of less than 125 km for most stations in cratonic settings, except those in Vs Cluster 2 which lie on the western edge of the continent. Xenolith data also indicate the presence of ancient, depleted lithosphere to depths of 150 km or more in cratonic settings, suggesting that at least in some instances the shallower discontinuity observed globally cannot be the LAB (Griffin et al., 1999; Jordan, 1978, 1988; Lee, 2006). In the remainder of this section we explore whether mechanisms such as melting and/or thermal changes, anisotropy or changes in composition can be invoked to explain the existence of MLDs.

Partial melting and then pooling within the lithosphere is one explanation for MLDs, although under ambient cratonic conditions there is no reason to expect that the geotherm will cross any solidi. Between roughly 75 and 120 km depth, there is a large high-temperature anomaly in central Australia between ~900°C and ~1,200°C (B. Kennett et al., 2018; Tesauro et al., 2020). The most likely cause of this large thermal anomaly is high crustal heat production observed in many Proterozoic terranes (>80 mW/m^2; McLaren et al., 2003). This corresponds with a region of increased conductivity at depths of 50–100 km in central Australia (L. Wang et al., 2014). Some of the MLDs observed in central Australia (MULG has an MLD at 75 km, WRAB has an MLD at 71 km, and WRKA has an MLD at 74 km) may be explained by this thermal anomaly, but other stations in central Australia (OOD, INKA) have MLDs either above or below this anomaly. Most of western and central Australia is relatively cold at MLD depths (300°C–500°C), indicating that a thermal anomaly is not able to explain the origin of MLDs in these regions (B. Kennett et al., 2018; Tesauro et al., 2020).

Previous studies have linked the presence of MLDs to anisotropy within the lithosphere (Bostock, 1998; Rychert & Shearer, 2009; Wirth & Long, 2014). In these cases, anisotropy is linked to previous tectonic events such as the formation of cratons and accretion of island arcs. In Australia, a large body of evidence exists to suggest the presence of complex and possibly layered anisotropy within the Australian lithosphere (Clitheroe & Van Der Hilst, 1998; Debayle et al., 2005; Heintz & Kennett, 2005; Yoshizawa, 2014; Yoshizawa & Kennett, 2015). Thus, it is possible that the MLDs we observed may be least partially due to anisotropy. However, the anisotropy observed in the upper 150 km of the lithosphere is in general weaker than below that (Debayle et al., 2005; Yoshizawa & Kennett, 2015). Previous forward modeling of RFs and synthetic seismograms has relied on 10%, though this is on the high end what is expected to occur naturally (Ford et al., 2016; Levin & Park, 1997, 1998; Wirth & Long, 2014). However, these are just models and the point at which anisotropy can produce an MLD may be slightly lower. The Australian lithosphere has strong anisotropy (~5%) down to at least 100 km, with moderate anisotropy (2%–3%) below that until asthenospheric depths where convection produces strong anisotropy again (Fouch & Rondenay, 2006; Yoshizawa, 2014; Yoshizawa & Kennett, 2015). There is no way to uniquely constrain anisotropy from this study, but analysis of the horizontal component of Ps receiver function can provide information about anisotropic boundaries. Forward modeling would help to constrain the needed amount of anisotropy to produce the conversions. If these boundaries occur at or near the same depth as the MLDs, then they may be explained by anisotropy, but these phenomena need not be linked (Ford et al., 2016).

Compositional changes are also frequently invoked to explain MLDs. One proxy for composition that is frequently used is known as the magnesium number (Mg#). This is defined as the amount of magnesium in a rock compared to the total magnesium and iron content in that rock (Mg# = Mg/(Mg + Fe) × 100). In

peridotites, which are the dominant composition of the upper mantle, Mg# ranges from ~86 to 88 for the primary composition and ~93 to 94 for more residual compositions such as those seen in cratonic settings. An increase in Mg# results in an increase in Vs (a roughly 2% increase between Mg# 88 and Mg#94) but causes no change in Vp; however, at standard temperate and pressure conditions Vp is weakly correlated with olivine abundance (Lee, 2003). B. Kennett et al. (2018) used a joint inversion of seismic and gravity data to produce a proxy for the Mg#. Their results show that while there are differences in the Mg# between the Phanerozoic east and the Precambrian west, there are not significant enough changes in Mg# with depth to explain the presence of MLDs, though this model is relatively coarse. Another recent study using the same technique found no significant variations through the cratons to depths of 300 km, with values ranging from 91.6 to 89.6 (Tesauro et al., 2020). This relatively small variation is not expected to produce a major velocity change. Paired with the 2% change in Vs compared to the observed 5%–7% needed to generate MLDs, this makes it unlikely that changes in Mg# are the primary cause of most MLDs observed in Australia.

One means of constraining changes in composition is from xenoliths originating from depths similar to the depths of MLDs, however, there are limited xenolith suites in Australia. Since the mid-Cretaceous there has been volcanism on the eastern margin of Australia related to plate motion and plume events (Davies & Rawlinson, 2014; Sutherland et al., 2012), but there has been no recent volcanism in the cratons. The only xenoliths found in these areas are from much older volcanism and are only useful if the MLDs are as old or older than the eruption. In the Kimberley Block of the NAC, xenoliths show an enriched mantle with hydrous minerals such as phlogopite; metasomatism in the mantle may explain the velocity drop associated with MLDs (Best, 1974; Edwards et al., 1992; Griffin et al., 1984; Konzett et al., 2013; McCulloch et al., 1983). Similarly, compatible element data from the Yilgarn Craton suggest that the mantle lithosphere was metasomatized before eruption around 2.025 Ga (Graham et al., 2004). Another study on xenoliths in the Yilgarn craton observed juvenile radiogenic isotopes and fluid-related trace element compositions, likely requiring the dehydration of a slab at 2.6–2.7 Ga (Choi et al., 2020). Saha et al. (2018) suggested that the presence of metasomatic minerals formed during subduction or other melting events (even if ancient) may explain the seismic velocity decrease associated with MLDs. If we observe metasomatic minerals in xenoliths that are ancient (in the case of Graham et al. (2004) the xenoliths are 2.025 Ga), it indicates that the conditions in the midlithosphere were conducive to the formation of zones of low velocity. If this is the case, then the MLDs themselves may be as old if not older than the xenoliths.

Aulbach, Massuyeau, and Gaillard (2017) argue that the most likely explanation for MLDs is the presence of hydrous minerals at depth. Their preferred mineral is phlogopite, which would create the observed seismic drop of ~5%–-7%. The origin of the phlogopite at MLD depths is still under debate: one possibility is that the phlogopite forms as a direct result of subduction and the introduction of hydrous fluids into the mantle (Konzett & Ulmer, 1999; Sato et al., 1997; Vielzeuf & Schmidt, 2001). However, other nontectonic processes may have helped hydrate the lithospheric mantle, such as interaction with a mantle plume. There is evidence from multiple cratons for the presence of hydrous minerals dating to the Precambrian, including the Australian cratons (Aulbach et al., 2007; Best, 1974; Choi et al., 2020; Edwards et al., 1992; Giuliani et al., 2016; Graham et al., 2004; Hopp et al., 2008; Konzett et al., 2013; Priyatkina et al., 2014). In addition, there is evidence for dipping seismic discontinuities in several cratons (Bostock, 1998; Chen, 2009; Cook et al., 1999; Cooper & Miller, 2014; Hopper & Fischer, 2015; Snyder, 2008) which has been linked to subduction in the Precambrian.

Alternatively, the presence of hydrous minerals may be linked to percolation of asthenospheric melt into the lithosphere, pooling around MLD depths (Aulbach, Massuyeau, & Gaillard, 2017; Rader et al., 2015). This does not invoke tectonic processes, and may instead be linked to the presence of plumes or other thermal perturbations. Indeed, at least one MLD in the North Atlantic Craton seems linked to the intrusion of kimberlites in the Mesozoic (Aulbach, Sun, et al., 2017). There is at least one suspected plume event in the Proterozoic (the ~1.6 Ga Hiltalba event) that may explain some of the hydrous minerals in the SAC and NAC (Betts et al., 2002). Additionally, in the Mesozoic, the western margin of Australia may have been affected by the Kerguelen Plume (Frey et al., 1996). This suggests that plumes cannot be ruled out as an origin for the hydrous minerals creating MLDs. Plumes are often cited as a model to generate cratonic lithosphere, wherein melt generated near the LAB may infiltrate and percolate to shallower depths (Lee et al., 2011). This model would also apply in subsequent interactions between craton and plumes, suggesting that

repeated events of melt infiltration may leave behind hydrous minerals at midlithospheric depths. Furthermore, it is presently thought that the sharp LAB observed in oceanic and younger continental lithosphere is linked to the presence of a small amount of partial melt in the asthenosphere (Fischer et al., 2010; Rychert et al., 2020), suggesting that thinner cratonic lithosphere in the past may have been well situated for melt percolation even without a plume or subduction, especially given that the mantle is predicted to have been hotter in the Precambrian (Herzberg et al., 2010).

Elastically accommodated grain-boundary sliding has also been suggested as a mechanism to explain MLDs (Karato, 2012; Karato et al., 2015). This mechanism requires at least a locally hydrated mantle and may thus be linked to the presence of metasomatic minerals at MLD depths. However, it is predicted that grain-boundary sliding occurs at ~1,000°C in olivine, yet most MLDs are seen in regions with temperatures predicted to be 700°C–900°C (Selway et al., 2015, and references therein). Selway et al. (2015) carried out a calculation using velocity profiles determined from the geotherm of the Kaapvaal craton (Artemieva, 2009), with average composition for an Archean craton (Griffin et al., 2009), and found that this mechanism does not produce the predicted and observed velocity discontinuities seen at MLD depths. It should be noted that the parameters involved in grain-boundary sliding are still poorly constrained and understood, and that this mechanism may operate in concert with the presence of hydrous minerals in the midlithosphere to create MLDs. However, it does not seem likely that grain-boundary sliding on its own can cause the ubiquitous and global MLDs.

We have presented a case above that MLDs observed in Australia cannot be uniquely explained by thermal causes, major changes in Mg# with depth, or anisotropy. In the case of the Australian MLDs, we argue that the most likely cause is the presence of hydrous minerals precipitated sometime in the Archean or Proterozoic, which are linked to either plate tectonic processes, plume interaction, or frozen melt that originated from partial melting at a paleo-LAB. These events are not mutually exclusive and may have acted together to form the MLDs. Furthermore, it is likely that these would require multiple episodes of melt infiltration and prolonged interaction.

5. Conclusions

We have performed an updated continental Sp and Ps receiver function analysis in Australia. Our findings generally mirror those in Ford et al. (2010), with shallow, sharp negative phases in Phanerozoic Australia predicted to be the LAB, and no obvious LAB with discrete velocity drops in the midlithosphere in cratonic Australia. Stations throughout Australia have multiple negative phases, suggesting a complex and possibly layered cratonic lithosphere. However, we do identify one cluster of stations in western Australia where both MLDs and potential LABs are observed.

We observe MLDs at depths between 61 and 118 km. The most likely explanation for Australian MLDs is the presence of hydrous minerals in the mantle. Xenoliths indicating hydrous minerals greater than 2 Ga in age suggest that MLDs originated in the Precambrian, possibly from plate tectonic processes, plume interaction, or melt infiltration from the paleo-LAB.

Data Availability Statement

Data from the AU, G, IU, II, and S1 seismic networks were accessed via the IRIS Data Management Center (http://ds.iris.edu/ds/nodes/dmc/data/types/waveform-data/).

Acknowledgments
This work was supported by National Science Foundation grant EAR-1620386 and the IRIS internship program. We would like to thank Kate Selway and one anonymous reviewer for their helpful comments and suggestions.

References

Abt, D. L., Fischer, K. M., French, S. W., Ford, H. A., Yuan, H., & Romanowicz, B. (2010). North American lithospheric discontinuity structure imaged by *Ps* and *Sp* receiver functions. *Journal of Geophysical Research*, *115*, B09301. https://doi.org/10.1029/2009JB006914

Artemieva, I. M. (2009). The continental lithosphere: Reconciling thermal, seismic, and petrologic data. *Lithos*, *109*(1–2), 23–46.

Auer, L., Boschi, L., Becker, T. W., Nissen-Meyer, T., & Giardini, D. (2014). *Savani*: A variable resolution whole-mantle model of anisotropic shear velocity variations based on multiple data sets. *Journal of Geophysical Research: Solid Earth*, *119*, 3006–3034. https://doi.org/10.1002/2013JB010773

Aulbach, S., Massuyeau, M., & Gaillard, F. (2017). Origins of cratonic mantle discontinuities: A view from petrology, geochemistry and thermodynamic models. *Lithos*, *268*, 364–382.

Aulbach, S., Pearson, N. J., O'reilly, S. Y., & Doyle, B. J. (2007). Origins of xenolithic eclogites and pyroxenites from the Central Slave Craton, Canada. *Journal of Petrology*, *48*(10), 1843–1873.

Aulbach, S., Sun, J., Tappe, S., Höfer, H. E., & Gerdes, A. (2017). Volatile-rich metasomatism in the cratonic mantle beneath SW Greenland: Link to kimberlites and mid-lithospheric discontinuities. *Journal of Petrology*, *58*(12), 2311–2338.

Baba, K., Chave, A. D., Evans, R. L., Hirth, G., & Mackie, R. L. (2006). Mantle dynamics beneath the East Pacific Rise at 17°S: Insights from the Mantle Electromagnetic and Tomography (MELT) experiment. *Journal of Geophysical Research*, *111*, B02101. https://doi.org/10.1029/2004JB003598

Barley, M. E., Loader, S. E., & McNaughton, N. J. (1998). 3430 to 3417 Ma calc-alkaline volcanism in the McPhee Dome and Kelly Belt, and growth of the eastern Pilbara Craton. *Precambrian Research*, *88*(1–4), 3–23.

Best, M. G. (1974). Mantle-derived amphibole within inclusions in alkalic-basaltic lavas. *Journal of Geophysical Research*, *79*(14), 2107–2113.

Betts, P. G., Giles, D., Lister, G. S., & Frick, L. R. (2002). Evolution of the Australian lithosphere. *Australian Journal of Earth Sciences*, *49*(4), 661–695.

Bodin, T., Yuan, H., & Romanowicz, B. (2014). Inversion of receiver functions without deconvolution—Application to the Indian craton. *Geophysical Journal International*, *196*(2), 1025–1033.

Bostock, M. G. (1998). Mantle stratigraphy and evolution of the Slave province. *Journal of Geophysical Research*, *103*(B9), 21183–21200.

Carlson, R. W., Pearson, D. G., & James, D. E. (2005). Physical, chemical, and chronological characteristics of continental mantle. *Reviews of Geophysics*, *43*, RG1001. https://doi.org/10.1029/2004RG000156

Cawood, P. A., & Korsch, R. J. (2008). Assembling Australia: Proterozoic building of a continent. *Precambrian Research*, *166*(1–4), 1–35.

Chen, C., Gilbert, H., Fischer, K. M., Andronicos, C. L., Pavlis, G. L., & Hamburger, M. W. (2018). Lithospheric discontinuities beneath the US Midcontinent–signatures of Proterozoic terrane accretion and failed rifting. *Earth and Planetary Science Letters*, *481*, 223–235.

Chen, L. (2009). Lithospheric structure variations between the eastern and central North China Craton from S- and P-receiver function migration. *Physics of the Earth and Planetary Interiors*, *173*(3–4), 216–227.

Choi, E., Fiorentini, M. L., Giuliani, A., Foley, S. F., Maas, R., & Taylor, W. R. (2020). Subduction-related petrogenesis of Late Archean calc-alkaline lamprophyres in the Yilgarn Craton (Western Australia). *Precambrian Research*, *338*, 105550.

Clitheroe, G., & Van Der Hilst, R. D. (1998). Complex anisotropy in the Australian lithosphere from shear-wave splitting in broad-band SKS records. *Structure and Evolution of the Australian Continent*, *26*, 73–78.

Conor, C. H., & Preiss, W. V. (2008). Understanding the 1720–1640 Ma Palaeoproterozoic Willyama Supergroup, Curnamona Province, Southeastern Australia: Implications for tectonics, basin evolution and ore genesis. *Precambrian Research*, *166*(1–4), 297–317.

Cook, F. A., van der Velden, A. J., Hall, K. W., & Roberts, B. J. (1999). Frozen subduction in Canada's Northwest Territories: Lithoprobe deep lithospheric reflection profiling of the western Canadian Shield. *Tectonics*, *18*(1), 1–24.

Cooper, C. M., & Miller, M. S. (2014). Craton formation: Internal structure inherited from closing of the early oceans. *Lithosphere*, *6*(1), 35–42.

Daly, S. J. (1998). Tectonic evolution and exploration potential of the Gawler Craton, South Australia. *AGSO Journal of Australian Geology and Geophysics*, *17*, 145–168.

Davies, D. R., & Rawlinson, N. (2014). On the origin of recent intraplate volcanism in Australia. *Geology*, *42*(12), 1031–1034.

Davies, D. R., Rawlinson, N., Iaffaldano, G., & Campbell, I. H. (2015). Lithospheric controls on magma composition along Earth's longest continental hotspot track. *Nature*, *525*(7570), 511–514.

Debayle, E., & Kennett, B. L. N. (2000). The Australian continental upper mantle: Structure and deformation inferred from surface waves. *Journal of Geophysical Research*, *105*(B11), 25423–25450.

Debayle, E., Kennett, B., & Priestley, K. (2005). Global azimuthal seismic anisotropy and the unique plate-motion deformation of Australia. *Nature*, *433*(7025), 509–512.

Demidjuk, Z., Turner, S., Sandiford, M., George, R., Foden, J., & Etheridge, M. (2007). U-series isotope and geodynamic constraints on mantle melting processes beneath the Newer Volcanic Province in South Australia. *Earth and Planetary Science Letters*, *261*(3–4), 517–533.

Direen, N. G., & Crawford, A. J. (2003). The Tasman Line: Where is it, what is it, and is it Australia's Rodinian breakup boundary? *Australian Journal of Earth Sciences*, *50*(4), 491–502.

Dueker, K., Yuan, H., & Zurek, B. (2001). Thick-structured Proterozoic lithosphere of the Rocky Mountain region. *Geological Society of America Today*, *11*(12), 4–9.

Eaton, D. W., Darbyshire, F., Evans, R. L., Grütter, H., Jones, A. G., & Yuan, X. (2009). The elusive lithosphere–asthenosphere boundary (LAB) beneath cratons. *Lithos*, *109*(1–2), 1–22.

Edwards, D., Rock, N. M. S., Taylor, W. R., Griffin, B. J., & Ramsay, R. R. (1992). Mineralogy and petrology of the Aries diamondiferous kimberlite pipe, Central Kimberley Block, Western Australia. *Journal of Petrology*, *33*(5), 1157–1191.

Evans, R. L., Hirth, G., Baba, K., Forsyth, D., Chave, A., & Mackie, R. (2005). Geophysical evidence from the MELT area for compositional controls on oceanic plates. *Nature*, *437*(7056), 249–252.

Evans, R. L., Jones, A. G., Garcia, X., Muller, M., Hamilton, M., Evans, S., et al. (2011). Electrical lithosphere beneath the Kaapvaal craton, southern Africa. *Journal of Geophysical Research*, *116*, B04105. https://doi.org/10.1029/2010JB007883

Fichtner, A., Kennett, B. L., Igel, H., & Bunge, H. P. (2010). Full waveform tomography for radially anisotropic structure: New insights into present and past states of the Australasian upper mantle. *Earth and Planetary Science Letters*, *290*(3–4), 270–280.

Fischer, K. M., Ford, H. A., Abt, D. L., & Rychert, C. A. (2010). The lithosphere–asthenosphere boundary. *Annual Review of Earth and Planetary Sciences*, *38*, 551–575.

Fishwick, S., Kennett, B. L. N., & Reading, A. M. (2005). Contrasts in lithospheric structure within the Australian Craton—Insights from surface wave tomography. *Earth and Planetary Science Letters*, *231*(3–4), 163–176.

Fishwick, S., & Rawlinson, N. (2012). 3-D structure of the Australian lithosphere from evolving seismic datasets. *Australian Journal of Earth Sciences*, *59*(6), 809–826.

Fishwick, S., & Reading, A. M. (2008). Anomalous lithosphere beneath the Proterozoic of western and central Australia: A record of continental collision and intraplate deformation? *Precambrian Research*, *166*(1–4), 111–121.

Ford, H. A., Fischer, K. M., Abt, D. L., Rychert, C. A., & Elkins-Tanton, L. T. (2010). The lithosphere–asthenosphere boundary and cratonic lithospheric layering beneath Australia from Sp wave imaging. *Earth and Planetary Science Letters*, *300*(3–4), 299–310.

Ford, H. A., Long, M. D., & Wirth, E. A. (2016). Midlithospheric discontinuities and complex anisotropic layering in the mantle lithosphere beneath the Wyoming and Superior Provinces. *Journal of Geophysical Research: Solid Earth*, *121*, 6675–6697. https://doi.org/10.1002/2016JB012978

Foster, K., Dueker, K., Schmandt, B., & Yuan, H. (2014). A sharp cratonic lithosphere–asthenosphere boundary beneath the American Midwest and its relation to mantle flow. *Earth and Planetary Science Letters*, *402*, 82–89.
Fouch, M. J., & Rondenay, S. (2006). Seismic anisotropy beneath stable continental interiors. *Physics of the Earth and Planetary Interiors*, *158*(2–4), 292–320.
Fraser, G. L., Huston, D., Gibson, G. M., Neumann, N. L., Maidment, D., Kositcin, N., et al. (2007). *Geodynamic and metallogenic evolution of Proterozoic Australia from 1870-1550 Ma: A discussion*. Symonston, Australia: Geoscience Australia.
Frey, F. A., McNaughton, N. J., Nelson, D. R., deLaeter, J. R., & Duncan, R. A. (1996). Petrogenesis of the Bunbury Basalt, Western Australia: Interaction between the Kerguelen plume and Gondwana lithosphere? *Earth and Planetary Science Letters*, *144*(1–2), 163–183.
Gaherty, J. B., Kato, M., & Jordan, T. H. (1999). Seismological structure of the upper mantle: A regional comparison of seismic layering. *Physics of the Earth and Planetary Interiors*, *110*(1–2), 21–41.
Gaillard, F., Malki, M., Iacono-Marziano, G., Pichavant, M., & Scaillet, B. (2008). Carbonatite melts and electrical conductivity in the asthenosphere. *Science*, *322*(5906), 1363–1365.
Gaul, O. F., O Reilly, S. Y., & Griffin, W. L. (2003). Lithosphere structure and evolution in southeastern Australia. *SPECIAL PAPERS-GEOLOGICAL SOCIETY OF AMERICA*, 185–202.
Giuliani, A., Phillips, D., Kamenetsky, V. S., & Goemann, K. (2016). Constraints on kimberlite ascent mechanisms revealed by phlogopite compositions in kimberlites and mantle xenoliths. *Lithos*, *240*, 189–201.
Gorbatov, A., Saygin, E., & Kennett, B. L. N. (2013). Crustal properties from seismic station autocorrelograms. *Geophysical Journal International*, *192*(2), 861–870.
Graham, S., Lambert, D., & Shee, S. (2004). The petrogenesis of carbonatite, melnoite and kimberlite from the Eastern Goldfields Province, Yilgarn Craton. *Lithos*, *76*(1–4), 519–533.
Griffin, W. L., Doyle, B. J., Ryan, C. G., Pearson, N. J., Suzanne, Y. O. R., & Davies, R. (1999). Layered mantle lithosphere in the Lac de Gras area, Slave craton: composition, structure and origin. *Journal of Petrology*, *40*(5), 705–727.
Griffin, W. L., O'reilly, S. Y., Afonso, J. C., & Begg, G. C. (2009). The composition and evolution of lithospheric mantle: A re-evaluation and its tectonic implications. *Journal of Petrology*, *50*(7), 1185–1204.
Griffin, W. L., Wass, S. Y., & Hollis, J. D. (1984). Ultramafic xenoliths from Bullenmerri and Gnotuk maars, Victoria, Australia: Petrology of a sub-continental crust–mantle transition. *Journal of Petrology*, *25*(1), 53–87.
Hales, A. L. (1969). A seismic discontinuity in the lithosphere. *Earth and Planetary Science Letters*, *7*(1), 44–46.
Hansen, S. M., Dueker, K. G., Stachnik, J. C., Aster, R. C., & Karlstrom, K. E. (2013). A rootless Rockies—Support and lithospheric structure of the Colorado Rocky Mountains inferred from CREST and TA seismic data. *Geochemistry, Geophysics, Geosystems*, *14*(8), 2670–2695.
Heintz, M., & Kennett, B. L. (2005). Continental scale shear wave splitting analysis: Investigation of seismic anisotropy underneath the Australian continent. *Earth and Planetary Science Letters*, *236*(1–2), 106–119.
Helffrich, G. (2006). Extended-time multitaper frequency domain cross-correlation receiver-function estimation. *Bulletin of the Seismological Society of America*, *96*(1), 344–347.
Herzberg, C., Condie, K., & Korenaga, J. (2010). Thermal history of the Earth and its petrological expression. *Earth and Planetary Science Letters*, *292*(1–2), 79–88.
Hirth, G., Evans, R. L., & Chave, A. D. (2000). Comparison of continental and oceanic mantle electrical conductivity: Is the Archean lithosphere dry? *Geochemistry, Geophysics, Geosystems*, *1*(12).
Hirth, G., & Kohlstedt, D. L. (1996). Water in the oceanic upper mantle: Implications for rheology, melt extraction and the evolution of the lithosphere. *Earth and Planetary Science Letters*, *144*(1–2), 93–108.
Hopp, J., Trieloff, M., Brey, G. P., Woodland, A. B., Simon, N. S. C., Wijbrans, J. R., et al. (2008). $^{40}Ar/^{39}Ar$-ages of phlogopite in mantle xenoliths from South African kimberlites: Evidence for metasomatic mantle impregnation during the Kibaran orogenic cycle. *Lithos*, *106*(3–4), 351–364.
Hopper, E., & Fischer, K. M. (2015). The meaning of midlithospheric discontinuities: A case study in the northern U.S. craton. *Geochemistry, Geophysics, Geosystems*, *16*, 4057–4083. https://doi.org/10.1002/2015GC006030
Hopper, E., & Fischer, K. M. (2018). The changing face of the lithosphere-asthenosphere boundary: Imaging continental scale patterns in upper mantle structure across the contiguous US with Sp converted waves. *Geochemistry, Geophysics, Geosystems*, *19*(8), 2593–2614.
Hopper, E., Ford, H. A., Fischer, K. M., Lekic, V., & Fouch, M. J. (2014). The lithosphere–asthenosphere boundary and the tectonic and magmatic history of the northwestern United States. *Earth and Planetary Science Letters*, *402*, 69–81.
Jordan, T. H. (1978). Composition and development of the continental tectosphere. *Nature*, *274*(5671), 544–548.
Jordan, T. H. (1988). Structure and formation of the continental tectosphere. *Journal of Petrology*, 11–37.
Karato, S. I. (2012). On the origin of the asthenosphere. *Earth and Planetary Science Letters*, *321*, 95–103.
Karato, S. I., & Jung, H. (1998). Water, partial melting and the origin of the seismic low velocity and high attenuation zone in the upper mantle. *Earth and Planetary Science Letters*, *157*(3–4), 193–207.
Karato, S. I., Olugboji, T., & Park, J. (2015). Mechanisms and geologic significance of the mid-lithosphere discontinuity in the continents. *Nature Geoscience*, *8*(7), 509–514.
Kennett, B., Chopping, R., & Blewett, R. (2018). *The Australian continent: A geophysical synthesis*. Canberra, Australia: ANU Press.
Kennett, B. L., Engdahl, E. R., & Buland, R. (1995). Constraints on seismic velocities in the Earth from traveltimes. *Geophysical Journal International*, *122*(1), 108–124.
Kennett, B. L., Fichtner, A., Fishwick, S., & Yoshizawa, K. (2013). Australian seismological reference model (AuSREM): Mantle component. *Geophysical Journal International*, *192*(2), 871–887.
Kennett, B. L., Fishwick, S., Reading, A. M., & Rawlinson, N. (2004). Contrasts in mantle structure beneath Australia: Relation to Tasman Lines? *Australian Journal of Earth Sciences*, *51*(4), 563–569.
Kennett, B. L. N. (2015). Lithosphere–asthenosphere P-wave reflectivity across Australia. *Earth and Planetary Science Letters*, *431*, 225–235.
Kennett, B. L. N., & Abdullah, A. (2011). Seismic wave attenuation beneath the Australasian region. *Australian Journal of Earth Sciences*, *58*(3), 285–295.
Kennett, B. L. N., & Furumura, T. (2016). Multiscale seismic heterogeneity in the continental lithosphere. *Geochemistry, Geophysics, Geosystems*, *17*, 791–809. https://doi.org/10.1002/2015GC006200
Kennett, B. L. N., & Liang, S. (2020). The transition from the Thomson Orogen to the North Australian Craton from seismic data. *Australian Journal of Earth Sciences*, 1–13.
Kennett, B. L. N., & Salmon, M. (2012). AuSREM: Australian seismological reference model. *Australian Journal of Earth Sciences*, *59*(8), 1091–1103.
Kennett, B. L. N., & Sippl, C. (2018). Lithospheric discontinuities in Central Australia. *Tectonophysics*, *744*, 10–22.

Kennett, B. L. N., Yoshizawa, K., & Furumura, T. (2017). Interactions of multi-scale heterogeneity in the lithosphere: Australia. *Tectonophysics*, *717*, 193–213.
Kind, R., Handy, M. R., Yuan, X., Meier, T., Kämpf, H., & Soomro, R. (2017). Detection of a new sub-lithospheric discontinuity in Central Europe with S-receiver functions. *Tectonophysics*, *700*, 19–31.
Kind, R., Yuan, X., & Kumar, P. (2012). Seismic receiver functions and the lithosphere–asthenosphere boundary. *Tectonophysics*, *536*, 25–43.
Konzett, J., & Ulmer, P. (1999). The stability of hydrous potassic phases in lherzolitic mantle—An experimental study to 9.5 GPa in simplified and natural bulk compositions. *Journal of Petrology*, *40*(4), 629–652.
Konzett, J., Wirth, R., Hauzenberger, C., & Whitehouse, M. (2013). Two episodes of fluid migration in the Kaapvaal craton lithospheric mantle associated with Cretaceous kimberlite activity: Evidence from a harzburgite containing a unique assemblage of metasomatic zirconium-phases. *Lithos*, *182*, 165–184.
Kumar, P., Kind, R., Yuan, X., & Mechie, J. (2012). USArray receiver function images of the lithosphere–asthenosphere boundary. *Seismological Research Letters*, *83*(3), 486–491.
Kumar, P., Yuan, X., Kumar, M. R., Kind, R., Li, X., & Chadha, R. K. (2007). The rapid drift of the Indian tectonic plate. *Nature*, *449*(7164), 894–897.
Lee, C. T. A. (2003). Compositional variation of density and seismic velocities in natural peridotites at STP conditions: Implications for seismic imaging of compositional heterogeneities in the upper mantle. *Journal of Geophysical Research*, *108*(B9), 2441. https://doi.org/10.1029/2003JB002413
Lee, C. T. A. (2006). Geochemical/petrologic constraints on the origin of cratonic mantle. *Geophysical Monograph-American Geophysical Union*, *164*, 89.
Lee, C. T. A., Lenardic, A., Cooper, C. M., Niu, F., & Levander, A. (2005). The role of chemical boundary layers in regulating the thickness of continental and oceanic thermal boundary layers. *Earth and Planetary Science Letters*, *230*(3–4), 379–395.
Lee, C. T. A., Luffi, P., & Chin, E. J. (2011). Building and destroying continental mantle. *Annual Review of Earth and Planetary Sciences*, *39*, 59–90.
Lekić, V., & Fischer, K. M. (2014). Contrasting lithospheric signatures across the western United States revealed by Sp receiver functions. *Earth and Planetary Science Letters*, *402*, 90–98.
Lekić, V., & Fischer, K. M. (2017). Interpreting spatially stacked Sp receiver functions. *Geophysical Journal International*, *210*(2), 874–886.
Levin, V., & Park, J. (1997). P-SH conversions in a flat-layered medium with anisotropy of arbitrary orientation. *Geophysical Journal International*, *131*(2), 253–266.
Levin, V., & Park, J. (1998). P-SH conversions in layered media with hexagonally symmetric anisotropy: A cookbook. In *Geodynamics of lithosphere & Earth's mantle* (pp. 669–697). Basel, Switzerland: Birkhäuser.
Levin, V., & Park, J. (2000). Shear zones in the Proterozoic lithosphere of the Arabian Shield and the nature of the Hales discontinuity. *Tectonophysics*, *323*(3–4), 131–148.
Liang, S., & Kennett, B. L. (2020). Passive seismic imaging of a craton edge—Central Australia. *Tectonophysics*, *797*, 228662.
Mancinelli, N. J., Fischer, K. M., & Dalton, C. A. (2017). How sharp is the cratonic lithosphere–asthenosphere transition? *Geophysical Research Letters*, *44*, 10189–10197. https://doi.org/10.1002/2017GL074518
McCulloch, M. T., Jaques, A. L., Nelson, D. R., & Lewis, J. D. (1983). Nd and Sr isotopes in kimberlites and lamproites from Western Australia: An enriched mantle origin. *Nature*, *302*(5907), 400–403.
McLaren, S., Sandiford, M., Hand, M., Neumann, N., Wyborn, L., & Bastrakova, I. (2003). The hot southern continent: Heat flow and heat production in Australian Proterozoic terranes. *Special Papers-Geological Society of America*, 157–168.
Myers, J. S. (1993). Precambrian history of the West Australian Craton and adjacent orogens. *Annual Review of Earth and Planetary Sciences*, *21*(1), 453–485.
Myers, J. S., Shaw, R. D., & Tyler, I. M. (1996). Tectonic evolution of Proterozoic Australia. *Tectonics*, *15*(6), 1431–1446.
Nettles, M., & Dziewoński, A. M. (2008). Radially anisotropic shear velocity structure of the upper mantle globally and beneath North America. *Journal of Geophysical Research*, *113*, B02303. https://doi.org/10.1029/2006JB004819
Park, J., & Levin, V. (2000). Receiver functions from multiple-taper spectral correlation estimates. *Bulletin of the Seismological Society of America*, *90*(6), 1507–1520.
Porritt, R. W., Miller, M. S., & Darbyshire, F. A. (2015). Lithospheric architecture beneath Hudson Bay. *Geochemistry, Geophysics, Geosystems*, *16*, 2262–2275. https://doi.org/10.1002/2015GC005845
Priyatkina, N., Khudoley, A. K., Ustinov, V. N., & Kullerud, K. (2014). 1.92 Ga kimberlitic rocks from Kimozero, NW Russia: Their geochemistry, tectonic setting and unusual field occurrence. *Precambrian Research*, *249*, 162–179.
Rader, E., Emry, E., Schmerr, N., Frost, D., Cheng, C., Menard, J., et al. (2015). Characterization and petrological constraints of the midlithospheric discontinuity. *Geochemistry, Geophysics, Geosystems*, *16*, 3484–3504. https://doi.org/10.1002/2015GC005943
Rawlinson, N., Pilia, S., Young, M., Salmon, M., & Yang, Y. (2016). Crust and upper mantle structure beneath southeast Australia from ambient noise and teleseismic tomography. *Tectonophysics*, *689*, 143–156.
Reading, A. M., & Kennett, B. L. N. (2003). Lithospheric structure of the Pilbara Craton, Capricorn Orogen and northern Yilgarn Craton, Western Australia, from teleseismic receiver functions. *Australian Journal of Earth Sciences*, *50*(3), 439–445.
Reading, A. M., Kennett, B. L. N., & Goleby, B. (2007). New constraints on the seismic structure of West Australia: Evidence for terrane stabilization prior to the assembly of an ancient continent? *Geology*, *35*(4), 379–382.
Reading, A. M., Tkalčić, H., Kennett, B. L., Johnson, S. P., & Sheppard, S. (2012). Seismic structure of the crust and uppermost mantle of the Capricorn and Paterson Orogens and adjacent cratons, Western Australia, from passive seismic transects. *Precambrian Research*, *196*, 295–308.
Ritsema, J., Deuss, A. A., Van Heijst, H. J., & Woodhouse, J. H. (2011). S40RTS: A degree-40 shear-velocity model for the mantle from new Rayleigh wave dispersion, teleseismic traveltime and normal-mode splitting function measurements. *Geophysical Journal International*, *184*(3), 1223–1236.
Romanowicz, B. (2009). The thickness of tectonic plates. *Science*, *324*(5926), 474–476.
Rychert, C. A., Harmon, N., Constable, S., & Wang, S. (2020). The nature of the lithosphere–asthenosphere boundary. *Journal of Geophysical Research: Solid Earth*, *125*, e2018JB016463. https://doi.org/10.1029/2018JB016463
Rychert, C. A., & Shearer, P. M. (2009). A global view of the lithosphere–asthenosphere boundary. *Science*, *324*(5926), 495–498.
Saha, S., Dasgupta, R., & Tsuno, K. (2018). High pressure phase relations of a depleted peridotite fluxed by CO_2–H_2O-bearing siliceous melts and the origin of mid-lithospheric discontinuity. *Geochemistry, Geophysics, Geosystems*, *19*, 595–620. https://doi.org/10.1002/2017GC007233
Salmon, M., Kennett, B. L. N., Stern, T., & Aitken, A. R. A. (2013). The Moho in Australia and New Zealand. *Tectonophysics*, *609*, 288–298.

Sato, K., Katsura, T., & Ito, E. (1997). Phase relations of natural phlogopite with and without enstatite up to 8 GPa: Implication for mantle metasomatism. *Earth and Planetary Science Letters*, *146*(3–4), 511–526.
Schaeffer, A. J., & Lebedev, S. (2013). Global shear speed structure of the upper mantle and transition zone. *Geophysical Journal International*, *194*(1), 417–449.
Selway, K., Ford, H., & Kelemen, P. (2015). The seismic mid-lithosphere discontinuity. *Earth and Planetary Science Letters*, *414*, 45–57.
Shen, X., Kim, Y., Song, T. R. A., & Lim, H. (2019). Data-oriented constraint on the interpretation of S receiver function and its application to observations of seismic discontinuities in the lithosphere–asthenosphere system. *Geophysical Journal International*, *219*(1), 496–513.
Simons, F. J., Zielhuis, A., & Van Der Hilst, R. D. (1999). The deep structure of the Australian continent from surface wave tomography. *Lithos*, *48*(1–4), 17–43.
Sleep, N. H. (2005). Evolution of the continental lithosphere. *Annual Review of Earth and Planetary Sciences*, *33*, 369–393.
Snyder, D. B. (2008). Stacked uppermost mantle layers within the Slave craton of NW Canada as defined by anisotropic seismic discontinuities. *Tectonics*, *27*, TC4006. https://doi.org/10.1029/2007TC002132
Sodoudi, F., Yuan, X., Kind, R., Lebedev, S., Adam, J. M. C., Kästle, E., & Tilmann, F. (2013). Seismic evidence for stratification in composition and anisotropic fabric within the thick lithosphere of Kalahari Craton. *Geochemistry, Geophysics, Geosystems*, *14*, 5393–5412. https://doi.org/10.1002/2013GC004955
Sun, W., Fu, L. Y., Saygin, E., & Zhao, L. (2018). Insights into layering in the cratonic lithosphere beneath Western Australia. *Journal of Geophysical Research: Solid Earth*, *123*, 1405–1418. https://doi.org/10.1002/2017JB014904
Sun, W., & Kennett, B. L. N. (2016). Receiver structure from teleseisms: Autocorrelation and cross correlation. *Geophysical Research Letters*, *43*, 6234–6242. https://doi.org/10.1002/2016GL069564
Sun, W., Zhao, L., Yuan, H., & Fu, L. Y. (2020). Sharpness of the midlithospheric discontinuities and craton evolution in North China. *Journal of Geophysical Research: Solid Earth*, *125*, e2019JB018594. https://doi.org/10.1029/2019JB018594
Sutherland, F. L., Graham, I. T., Meffre, S., Zwingmann, H., & Pogson, R. E. (2012). Passive-margin prolonged volcanism, East Australian Plate: Outbursts, progressions, plate controls and suggested causes. *Australian Journal of Earth Sciences*, *59*(7), 983–1005.
Tesauro, M., Kaban, M. K., & Aitken, A. R. (2020). Thermal and compositional anomalies of the Australian upper mantle from seismic and gravity data. *Geochemistry, Geophysics, Geosystems*, *21*, e2020GC009305. https://doi.org/10.1029/2020GC009305
Tharimena, S., Rychert, C. A., & Harmon, N. (2016). Seismic imaging of a mid-lithospheric discontinuity beneath Ontong Java Plateau. *Earth and Planetary Science Letters*, *450*, 62–70.
Thybo, H. (2006). The heterogeneous upper mantle low velocity zone. *Tectonophysics*, *416*(1–4), 53–79.
Vielzeuf, D., & Schmidt, M. W. (2001). Melting relations in hydrous systems revisited: Application to metapelites, metagreywackes and metabasalts. *Contributions to Mineralogy and Petrology*, *141*(3), 251.
Wang, L., Hitchman, A. P., Ogawa, Y., Siripunvaraporn, W., Ichiki, M., & Fuji-ta, K. (2014). A 3-D conductivity model of the Australian continent using observatory and magnetometer array data. *Geophysical Journal International*, *198*(2), 1143–1158.
Wei, Z., Kennett, B. L., & Sun, W. (2018). Sn-wave velocity structure of the uppermost mantle beneath the Australian continent. *Geophysical Journal International*, *213*(3), 2071–2084.
Wilson, D. C., Angus, D. A., Ni, J. F., & Grand, S. P. (2006). Constraints on the interpretation of S-to-P receiver functions. *Geophysical Journal International*, *165*(3), 969–980.
Wirth, E. A., & Long, M. D. (2014). A contrast in anisotropy across mid-lithospheric discontinuities beneath the central United States—A relic of craton formation. *Geology*, *42*(10), 851–854.
Wittlinger, G., & Farra, V. (2007). Converted waves reveal a thick and layered tectosphere beneath the Kalahari super-craton. *Earth and Planetary Science Letters*, *254*(3–4), 404–415.
Wölbern, I., Rümpker, G., Link, K., & Sodoudi, F. (2012). Melt infiltration of the lower lithosphere beneath the Tanzania craton and the Albertine rift inferred from S receiver functions. *Geochemistry, Geophysics, Geosystems*, *13*, Q0AK08. https://doi.org/10.1029/2012GC004167
Yoshizawa, K. (2014). Radially anisotropic 3-D shear wave structure of the Australian lithosphere and asthenosphere from multi-mode surface waves. *Physics of the Earth and Planetary Interiors*, *235*, 33–48.
Yoshizawa, K., & Kennett, B. L. N. (2015). The lithosphere–asthenosphere transition and radial anisotropy beneath the Australian continent. *Geophysical Research Letters*, *42*, 3839–3846. https://doi.org/10.1002/2015GL063845
Yuan, H., & Romanowicz, B. (2010). Lithospheric layering in the North American craton. *Nature*, *466*(7310), 1063–1068.
Zhu, L., & Kanamori, H. (2000). Moho depth variation in southern California from teleseismic receiver functions. *Journal of Geophysical Research: Solid Earth*, *105*(B2), 2969–2980.